JGR Solid Earth

RESEARCH ARTICLE
10.1029/2018JB017188

Key Points:
- Geomorphology and paleoseismic trenching suggest Holocene slip along El Yolki fault in Central Chile despite absence of surface ruptures
- A 4.3-ka sequence of intertidal sediments has been uplifted ~10 m along the footwall fault block
- Crustal faulting may be triggered by megathrust events with slip distribution different from the last M8.8 earthquake in 2010

Supporting Information:
- Supporting Information S1
- Data Set S1
- Data Set S2
- Data Set S3

Correspondence to:
D. Melnick,
daniel.melnick@uach.cl

Citation:
Melnick, D., Hillemann, C., Jara-Muñoz, J., Garrett, E., Cortés-Aranda, J., Molina, D., et al. (2019). Hidden Holocene slip along the coastal El Yolki fault in Central Chile and its possible link with megathrust earthquakes. *Journal of Geophysical Research: Solid Earth*, *124*, 7280–7302. https://doi.org/10.1029/2018JB017188

Received 18 DEC 2018
Accepted 13 JUN 2019
Accepted article online 23 JUN 2019
Published online 9 JUL 2019
Corrected 15 AUG 2019

This article was corrected on 15 AUG 2019. See the end of the full text for details.

Hidden Holocene Slip Along the Coastal El Yolki Fault in Central Chile and Its Possible Link With Megathrust Earthquakes

Daniel Melnick[1,2,3], Christian Hillemann[3], Julius Jara-Muñoz[2,3], Ed Garrett[4], Joaquín Cortés-Aranda[2,5], Diego Molina[2,5], Andrés Tassara[2,5], and Manfred R. Strecker[3]

[1]Instituto de Ciencias de la Tierra, TAQUACh, Universidad Austral de Chile, Valdivia, Chile, [2]Millennium Nucleus The Seismic Cycle Along Subduction Zones, Valdivia, Chile, [3]Institute of Geosciences, University of Potsdam, Potsdam, Germany, [4]Department of Geography, Durham University, Durham, UK, [5]Departamento de Ciencias de la Tierra, Universidad de Concepción, Concepción, Chile

Abstract Megathrust earthquakes are commonly accompanied by increased upper-plate seismicity and occasionally triggered fault slip. In Chile, crustal faults slipped during and after the 2010 Maule (M8.8) earthquake. We studied the El Yolki fault (EYOF), a transtensional structure midways the Maule rupture not triggered in 2010. We mapped a Holocene coastal plain using light detection and ranging, which did not reveal surface ruptures. However, the inner-edge and shoreline angles along the coastal plain as well as 4.3- to 4.0-ka intertidal sediments are back-tilted on the EYOF footwall block, documenting 10 m of vertical displacement. These deformed markers imply ~2-mm/year throw rate, and dislocation models a slip rate of 5.6 mm/year for the EYOF. In a 5-m-deep trench, the Holocene intertidal sediments onlap to five erosive steps, interpreted as staircase wave-cut landforms formed by discrete events of relative sea level drop. We tentatively associated these steps with coseismic uplift during EYOF earthquakes between 4.3 and 4.0 ka. The Maule earthquake rupture may be subdivided into three subsegments based on coseismic slip and gravity anomalies. Coulomb stress transfer models predict neutral stress changes at the EYOF during the Maule earthquake but positive changes for a synthetic slip distribution at the central subsegment. If EYOF earthquakes were triggered by megathrust events, their slip distribution was probably focused in the central subsegment. Our study highlights the millennial variability of crustal faulting and the megathrust earthquake cycle in Chile, with global implications for assessing the hazards posed by hidden but potentially seismogenic coastal faults along subduction zones.

1. Introduction

In subduction zones, the locus of great earthquakes, forearc deformation has been commonly linked to the interplate megathrust seismic cycle, the locus of great earthquakes (e.g., Cubas et al., 2013; Dinther et al., 2013; Fuller et al., 2006; Loveless et al., 2010; Rosenau et al., 2009; Upton et al., 2003; Wang & Hu, 2006). Mechanical models supported by geodetic measurements show that many forearcs will experience broadly distributed shortening in response to locking of the interplate megathrust during the interseismic phase of the seismic cycle. In turn, the tectonic stress regime across forearcs during coseismic deformation caused by a megathrust earthquake will largely depend on the location of interplate slip, with potentially alternating areas of contraction and extension within the rupture zone (e.g., Li et al., 2014; Wang & Hu, 2006).

Crustal faults have been mapped in most, if not all forearc regions bounding subduction zones, and their movement has often been associated with triggered slip by megathrust earthquakes (e.g., Audin et al., 2008; Clarke & Carver, 1992; Cortés et al., 2012; Farias et al., 2011; McCaffrey & Goldfinger, 1995; Melnick, Moreno, Motagh, et al., 2012; Park et al., 2002; Plafker, 1965). In fact, the kinematic response of upper-plate faults to slip during a megathrust earthquake will depend on their location with respect to the locus of plate-boundary slip (Li et al., 2014). For example, crustal faults located along the outer forearc will be more commonly reactived with reverse kinematics, such as the Montague and Patton Bay faults triggered by the 1964 Alaska (M9.2) earthquake (Plafker, 1965) and the Santa María fault triggered during the 2010 Maule (M8.8) earthquake (Melnick, Moreno, Motagh, et al., 2012); conversely, those faults located farther inland above deeper portions of the seismogenic zone may rather experience extensional reactivations, such as the Yunodake and Itozawa faults triggered by the 2011 Tohoku (M9.1) earthquake (Toda

& Tsutsumi, 2013) and the Pichilemu fault triggered by the Maule earthquake (Aron et al., 2013; Farias et al., 2011).

Based on an analysis of seismicity catalogues, Gomberg and Sherrod (2014) concluded that the rate of upper-plate seismicity following great subduction earthquakes (Mw>8.6) records an overall increase with respect to background activity. A similar conclusion was reached by Sherrod and Gomberg (2014) from the study of prehistoric earthquake records, further emphasizing the proposed causal relation. Because of the shallow depth of upper-plate earthquakes, which mostly affect coastal areas that host densely populated regions, these forearc earthquakes may cause pronouced localized damage (Ten Brink & Lin, 2004). The recurrence of such coastal earthquakes may reach several thousand years (Toda & Tsutsumi, 2013) and therefore exceed the length of instrumental and available historical records. Despite these problems regarding unambiguous information on past earthquakes, paleoseismic archives may provide the only constraint to properly assess seismic hazards associated with such structures in the realm of plate-boundary faults. In addition, the study of subsidiary crustal faults may provide insight into the variability of slip distribution during megathrust earthquakes as mechanical models predict that faults suitably oriented to stress changes are prone to experiencing triggered slip (Li et al., 2014).

Permanent forearc deformation has been commonly associated with slip on upper-plate faults triggered by great subduction earthquakes, supported by observations along modern and fossil margins (e.g., Aron et al., 2013; Cortés-Aranda et al., 2015; Dielforder et al., 2015; Hasegawa et al., 2012; Jara-Muñoz et al., 2017; Toda & Tsutsumi, 2013). In order to gain empirical insight on the processes linking great megathrust earthquakes and upper-plate deformation as well as to improve hazard models, we studied the El Yolki fault (EYOF) located midway along the coast affected by the 2010 Maule earthquake. The fault was identified and first mapped during a regional survey using airborne light detection and ranging (LiDAR) data, and its Quaternary activity was corroborated by vertically displaced marine terraces from the last interglacial period (Jara-Muñoz et al., 2015). Here we document Holocene activity along the EYOF and estimate its slip rate using geologic and geomorphic mapping, paleoseismic trenching, microfossil analysis, radiocarbon dating, and numerical modeling. We frame our results within ongoing discussions relating segmentation of megathrust earthquakes and upper-plate deformation along subduction zones.

2. Tectonic and Geologic Setting

2.1. Morphotectonic Framework

The Chile margin is characterized by convergence of the oceanic Nazca plate below South America at 66 mm/a (e.g., Angermann et al., 1999). Throughout most of the Cenozoic, the margin has been affected by subduction erosion and upper-plate extension, resulting in a series of forearc basins filled with marine and continental sediments (Mordojovich, 1981). South of 33°S, the margin changed to an accretionary mode after onset of Patagonian glaciations and increased trenchward sediment transport in the late Miocene (Bangs & Cande, 1997). As a consequence, forearc basins suffered moderate inversion (Melnick & Echtler, 2006), documented by local reverse motion along a limited number of former normal faults. However, extension has persisted along some forearc faults, apparently associated with triggered slip during megathrust earthquakes (Aron et al., 2013).

The onshore forearc includes narrow Holocene coastal plains and uplifted Pleistocene marine terraces along the western flank of the up to ~1-km-high Coastal Cordillera (Figure 1). This range consists of Paleozoic metamorphic and intrusive basement rocks covered by isolated Cretaceous to recent marine and continental deposits. The basement constitutes a paleo-accretionary wedge associated with pervasive ductile and brittle deformation characteristics (e.g., Glodny et al., 2005; Glodny et al., 2006; Hervé et al., 1988; Martin et al., 1999; Willner, 2005). The Central Valley, along the eastern inland flank of the Coastal Cordillera, hosts mostly undeformed Cenozoic to Quaternary sediments affected by a few local and minor faults with subdued displacements (Lavenu & Cembrano, 1999; Rehak et al., 2008; Rehak et al., 2010).

2.2. Quaternary Faults Along the Chile Forearc

Although crustal faults are ubiquitous in every tectonic province of Chile, Quaternary structures have been studied mostly in the forearc region (e.g., Allmendinger et al., 2005; Allmendinger & González, 2010; Cortés et al., 2012; Ewiak et al., 2015; González et al., 2006; Jara-Muñoz et al., 2015; Lin et al.,

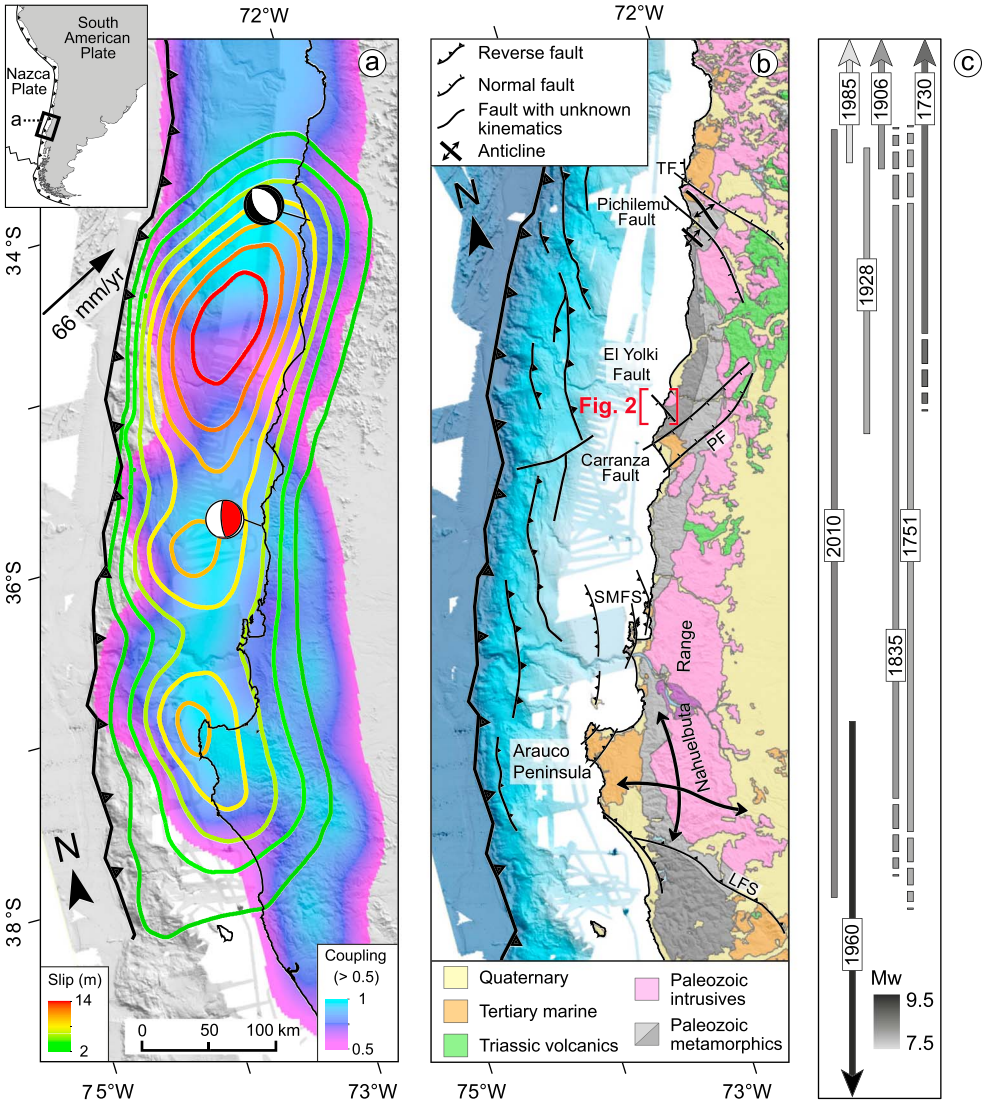

Figure 1. Regional setting. (a) Coseismic slip during the 2010 Maule earthquake (2-m contours) and interseismic coupling before the event (Moreno et al., 2012). The red and black focal mechanisms show Maule and Pichilemu earthquakes, respectively. (b) Simplified geologic map and Quaternary faults, modified from Jara-Muñoz et al. (2015 and reference therein). PFS: Pichilemu Fault; LFS: Lanalhue Fault; EYOF: El Yolki Fault; PF: Pelluhue Fault; CF: Carranza Fault; SMFS: Santa María Fault System. (c) Inferred rupture zones of historical megathrust earthquakes (see text for details and sources).

2016; Marquardt et al., 2004; Melnick et al., 2006; Melnick et al., 2009; Melnick, Moreno, Motagh, et al., 2012; Pérez et al., 2014; Vargas et al., 2013; Vargas et al., 2014). Along the coast of south-central Chile, crustal-scale faults associated with clusters of shallow microseismicity and deformed Quaternary geomorphic features have predominantly reverse kinematics (Jara-Muñoz et al., 2015; Jara-Muñoz et al., 2017; Melnick et al., 2009). In turn, farther north in central Chile, most faults that intersect the coastline have extensional kinematics and are not associated with such high topography, with only a few contractional structures affecting Quaternary sediments (Lavenu & Encinas, 2005). Several Quaternary normal faults have been mapped at a regional scale, which markedly offset marine terraces from the Marine Isotope Stages (MIS) 5 (Jara-Muñoz et al., 2015); however, virtually nothing is known regarding their Holocene slip rate and seismic potential. The lack of knowledge is underscored by the case of the Pichilemu fault, an extensional structure with pronounced geomorphic expression that had not been identified as being active and properly mapped until it generated two Mw 6.9 and 7.0 shallow earthquakes 11

days after the 2010 Maule megathrust event (e.g., Farias et al., 2011; Ruiz et al., 2014; Ryder et al., 2012). These two crustal earthquakes were not associated with clear surface ruptures and left no imprint in the geologic record. So far, no evidences for Holocene surface ruptures have been found along the Pichilemu Fault in the context of fault triggering during megathrust earthquakes; this setting highlights the urgent need to identify, map, and estimate the seismic potential of faults using deformed geomorphic markers; it also emphasizes the continued search for alternative paleoseismic records to derive a proper hazard assessment.

The EYOF region is located south of Pichilemu and characterized by three Quaternary faults (Figure 1). At ~35.5°S, the NE-SW striking Pelluhue and Carranza faults constitute reactivated structures bounding a Cretaceous graben; these faults have slipped with throw rates of 0.2 and 0.4 mm/year, respectively, as determined from offsets of the MIS-5e (~125 ka) marine terrace (Jara-Muñoz et al., 2015). Located ~20 km north of Carranza, the EYOF is an ~10-km-long, NW-SE striking, SW dipping structure that apparently splays from the Carranza fault (Figure 1). The EYOF likely extends farther offshore for an unknown length. All of these structures were first recognized during a regional survey of marine terraces and Quaternary faults along the Maule earthquake segment using bare-earth digital terrain models derived from airborne LiDAR data and field observations (Jara-Muñoz et al., 2015).

2.3. Historical Subduction Earthquakes in South-Central Chile

Historical earthquake records in the region extend back to 1570 and document the recurrence of several great events every century (Lomnitz, 2004). The largest earthquake that affected the EYOF region occurred in 1730 and had an estimated Mw of 9, based on the analysis of tsunami records in Chile and Japan (Carvajal et al., 2017). The EYOF region is located in the northern half of the 2010 Maule earthquake that had a total rupture length of ~500 km and a Mw of 8.8 (Figure 1a). The 2010 event was characterized by a complex slip distribution with two main patches with peak slip of ~17 and ~12 m at the northern and southern sectors of the rupture, respectively (Lin et al., 2013; Moreno et al., 2012; Tong et al., 2010). The 2010 earthquake was preceded by a similar event in 1835, described by Darwin and FitzRoy during the voyage of the Beagle; that event had an analogous rupture area and magnitude as suggested by land-level changes (Melnick, Moreno, Cisternas, & Tassara, 2012; Wesson et al., 2015).

Little is known about the prehistoric predecessors of the 1730 and 2010 earthquakes. At Quintero (33°S), Dura et al. (2015) found evidence for six mid Holocene M>8.5 earthquakes that possibly resembled the 1730 event. In the Maule segment, two adjacent sites (Tirúa and Quidico), located at the southernmost tip of the 2010 rupture (38.3°S), include geologic records of two prehistoric earthquakes with similar land-level changes and tsunami deposits as the Maule event in AD1425-1455 and AD1455-1570 (Dura et al., 2017).

The slip distribution of the 2010 Maule earthquake showed that the rupture was subdivided in three segments (Moreno et al., 2012): a southern region with peak slip greater than 10 m below the Arauco Peninsula resulted in coastal uplift that reached ~2 m at Lebu (Melnick, Cisternas, Moreno, & Norambuena, 2012), a central segment where slip was less than 10 m and no significant coastal land-level changes, and the northern segment where slip was located mostly offshore reaching ~17 m and resulting in less than 0.5 m of coastal subsidence (Farías et al., 2010).

3. Material and Methods

3.1. Geomorphic Mapping

In order to map the onshore surface expression of the EYOF based on deformed geomorphic features, we used a 2.5-m digital terrain model (DTM) derived from airborne LiDAR data at regional scale (Figure 2) and a 1-m DTM at local scale (Figure 3), both acquired by Digimapas Chile (www.digimapas.cl). We used the DTMs as a base for geologic and geomorphic field mapping (Data Set S1 in the supporting information). During our search for promising trenching locations, we deployed a Riegl LMS-Z260 long-range terrestrial laser scanner capturing 85 million points from 12 scan positions along the coastal plain. The point cloud was processed using the LAStools software (www.rapidlasso.com) to filter out vegetation (Data Set S2).

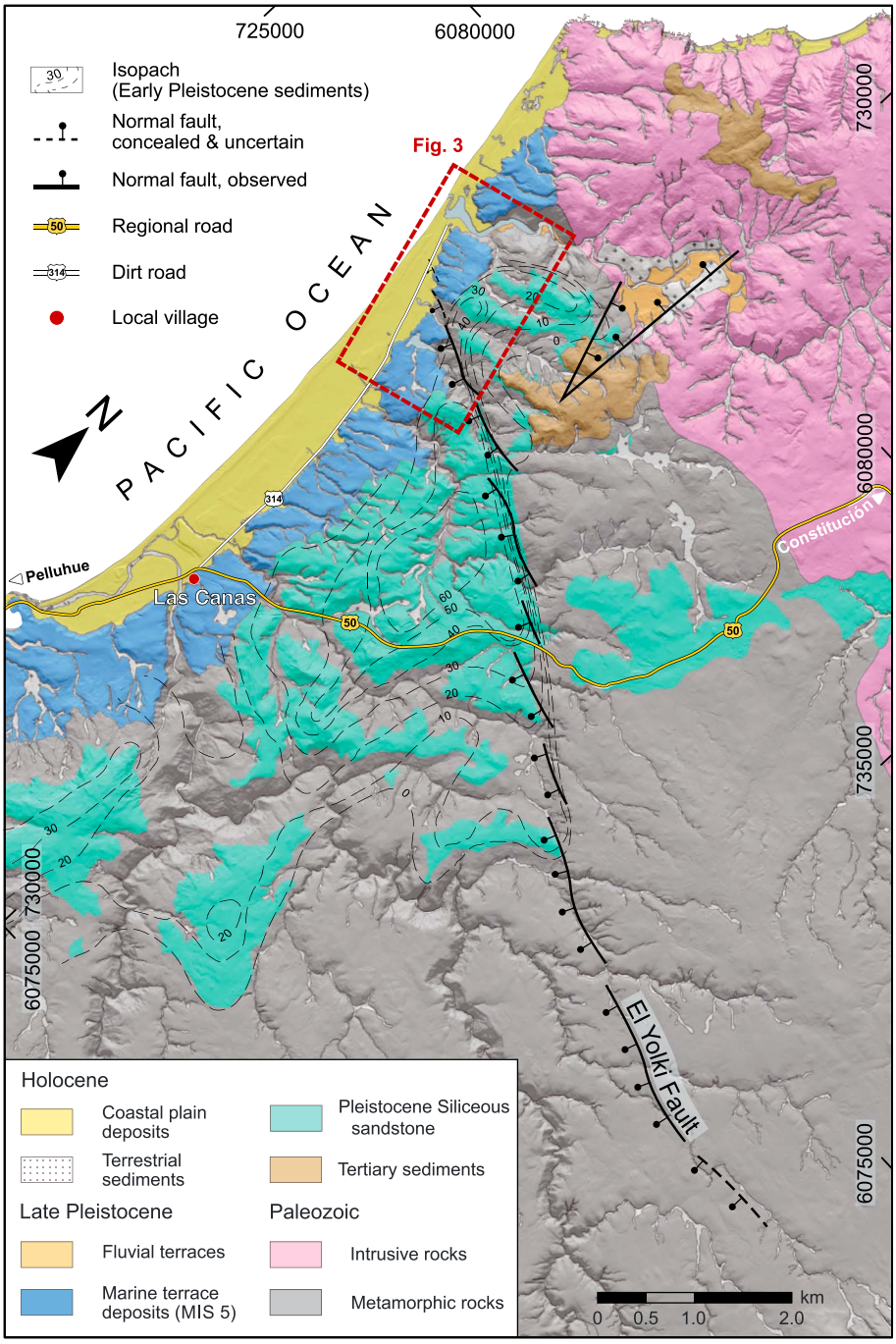

Figure 2. Regional structural geologic map of the El Yolki Fault over shaded-relief Digital Terrain Model from airborne light detection and ranging data, modified from Jara-Muñoz et al. (2015).

To link the older Holocene environments with their modern counterparts, we referred all the elevation data sets to a common tidal datum. We used a differential Global Navigation Satellite Systems (Leica Viva) to survey terrestrial scanner positions, trenches, and tide levels. These levels were obtained at an adjacent rocky coast site during three time windows over a period of 13 days; using the TPXO 8 Atlas tidal model (Egbert & Erofeeva, 2002), we converted EGM2008 elevations to mean tide level by substracting the mean difference between measured and modeled tides. The TPXO model has been validated with local tide gauge data from the south-central Chilean coast (Melnick, Cisternas, Moreno, & Norambuena, 2012). Though the

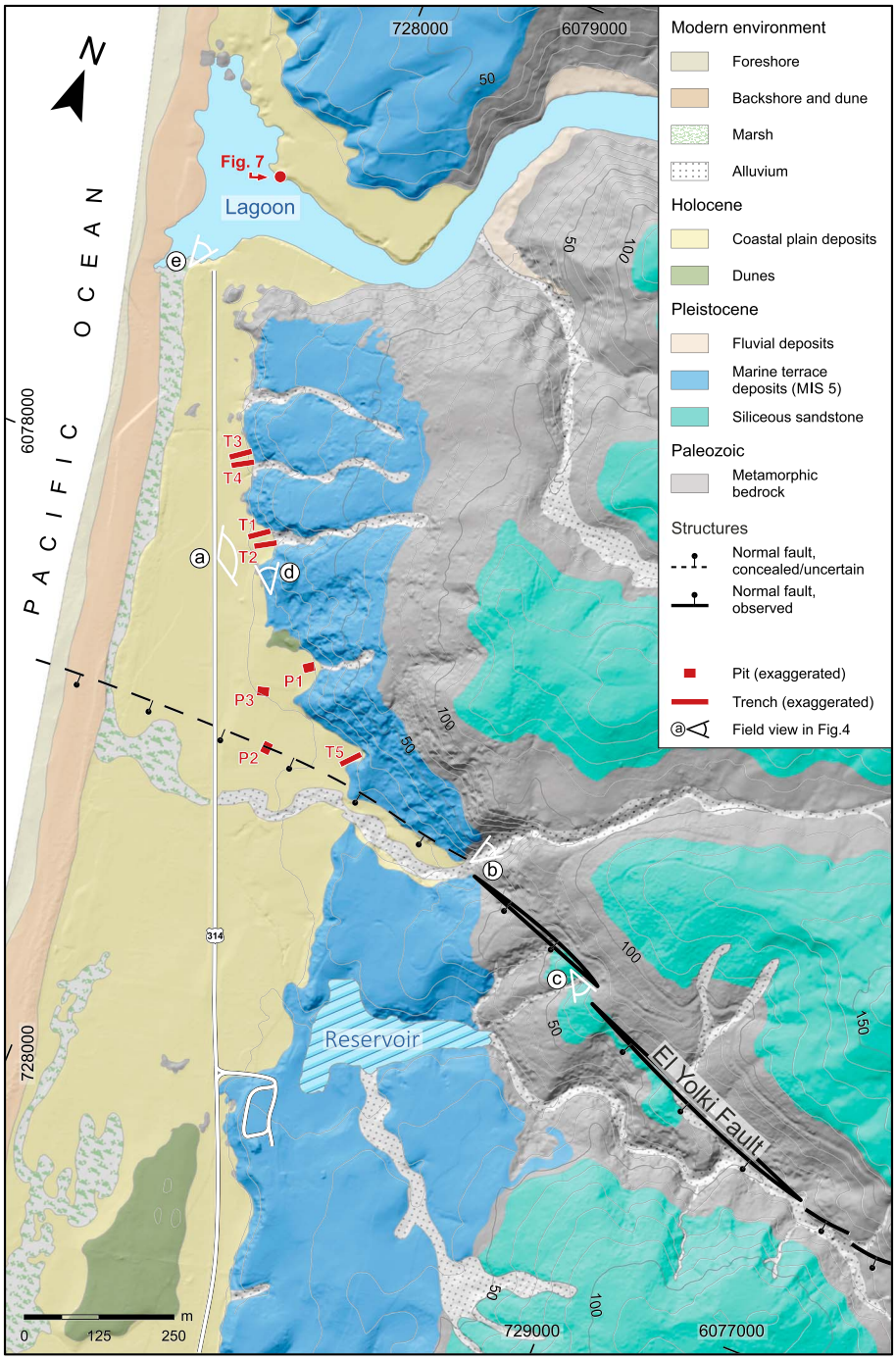

Figure 3. Detailed geologic map of the coastal plain and El Yolki fault; outline of geological units draped over shaded-relief bare-earth digital terrain model from airborne light detection and ranging data. The circled letters indicate location of field views in Figure 4.

TPXO model effectively predicts ocean tides, nonharmonic influences on sea surface heights such as wind-related drag, the inverted barometer effect, or longer-term water temperature variations associated with El Niño-Southern Oscillation are not considered. These effects are well within the uncertainties of the model and have been discarded in line with similar studies (e.g., Melnick, Cisternas, Moreno, & Norambuena, 2012; Meltzner et al., 2006). Local bathymetric effects along the relatively simple and straight coastline adjacent to the EYOF are expected to be minor. The mean offset between measured and modeled tide

levels was 8.5 ± 6.8 cm (1σ); tide levels and tidal model plots may be found in Figure S1 in the supporting information. All the elevation values given in this study are referred to the TPXO 8 mean tide level (mtl) datum.

To quantify footwall deformation associated with slip along the EYOF, we mapped the inner edge and shoreline angle of the Holocene coastal plain. Inner edges were estimated by mapping the foot of the Holocene sea cliff using a Surface Classification Model (Bowles & Cowgill, 2012) calculated from the LiDAR DTM (Figure S6). Elevations of Holocene shoreline angles were obtained with the TerraceM software (Jara-Muñoz et al., 2016) at 25 locations (Figure S6 and Data Set S3 in the supporting information).

3.2. Trenching, Geochronology, and Stratigraphic Model

In the search for geologic records of Holocene deformation, we first dug 10 exploration pits of variable sizes along the uplifted footwall block of the EYOF, at the transition between seaward facing slopes and in situ bedrock outcrops, characterized by metric-scale scarps (Figure 3). Based on the findings of uplifted poorly consolidated sediments of marine origin, five pits were extended into 4 trenches, 1.5-m wide, dug with an excavator (Figures 3 and 4d). These include the 12-m long and up to 5-m deep principal trench (T1) as well as three auxiliary trenches (T3, T4, and T5). A 0.5-m-grid was installed on the trench walls for logging and to tie a photomosaics composed of hundreds of single shots with ~75% overlap (Figure S2). Three-dimensional digital models of trench walls were generated using Structure-from-Motion techniques. Detailed descriptions of the sedimentary facies in T1 may be found in Figure S3.

To reconstruct the depositional history and timing of uplift of the Holocene sediments exposed in the trenches and adjacent lagoon, we collected 21 samples of charcoal, plant remains, and bones for radiocarbon dating (Table 1). Ages in T1 were calibrated using the ShCal13 curve (Hogg et al., 2013) and modeled with respect to their stratigraphic position using a Bayesian approach (P_Sequence) with OxCal V4.2 (Ramsey, 1995). Apparent age reversals in T1 result from the seaward dip of the sedimentary units (Figure 5). In order to account for this dip, the depth in the sedimentary section has been measured from the top perpendicular to the local bedding dip.

3.3. Microfossil Analysis

Quantifying diatom assemblage composition provides information on depositional environments and sediment sources (Shennan et al., 1996). Diatoms, silica-based algae found in aquatic environments, occupy restricted niches controlled by variables such as salinity, frequency of tidal inundation, and nutrient availability (Vos & de Wolf, 1993). Using standard preparation methods (Palmer & Abbott, 1986), we quantified diatom assemblages in four samples (sample details in Text S1 and Table S1 in the supporting information). We inspected slides at a magnification of x1000 and identified at least 250 diatom valves from each sample. Species identifications are based on reference material held by Durham University, UK. Ecological inferences are drawn from comparisons with a database of modern Chilean intertidal species from >250 samples taken from tidal marsh sites between ~39 and 42°S (Garrett et al., 2013; Hocking et al., 2017). The data set includes samples throughout the tidal frame but does not include subtidal or many supratidal samples. Dissimilarity between the fossil assemblages and the modern samples limits the use of transfer function approaches to provide precise paleo-elevations; instead, we explore the preferred elevations inhabited by each fossil species in the modern data set. Elevation optima and associated tolerances are derived through weighted averaging using the C2 software package (Juggins, 2007) and are expressed in Standardized Water Level Index Units. The use of this index allows comparison of sites with different tidal ranges; at each site a SWLI value of 100 corresponds to mean sea level; 200 corresponds to mean higher high water (MHHW). Using the TPXO8 model, we estimated MHHW at El Yolki to be 0.6 m amtl, which is within the range of other studied sites along the coast of south-central Chile (Garrett et al., 2013; Hocking et al., 2017).

3.4. Fault-Slip Rate Determination Using Elastic Dislocation Models

In order to estimate the Holocene fault-slip rate of the EYOF we used deformed index markers—samples that have similar radiocarbon ages and a common paleo-elevation as inferred from diatom assemblages. In addition, we used deformed geomorphic markers (inner edge and shoreline angle of the Holocene coastal plain) to fit models based on the dislocation theory of a buried fault in an elastic half-space (Okada, 1985), applied to a shallow crustal fault of poorly known subsurface structure (de Gelder et al., 2019; Melnick

Figure 4. Field views of geologic and geomorphic features associated with the El Yolki fault (EYOF), locations in Figure 3. (a) Panoramic view of tilted MIS-5 terrace and Holocene coastal plain. Trench locations are indicated by red dots. The stippled line shows base of Holocene paleo-cliff. (b) Outcrop of fractured metamorphic bedrock adjacent to the EYOF. (c) View of NW-SE striking fault scarp affecting Pleistocene siliceous sandstone. (d) View of T1 trenching location with excavator. (e) Panoramic view of the modern lagoon, MIS-5 terrace, Holocene coastal plain and associated geomorphic features.

et al., 2017; Resor, 2008). The sediments exposed at trench T1 and the lagoon outcrop (see sections 4.2.1 and 4.2.2) have a similar 4.3-ka age and common paleo-elevation around MHHW as inferred from their diatom contents. In addition, the base of trench T2 exposed similar sediments with equivalent ages. Even though the diatom content of sediments in T2 was not studied, we infer an analogous sedimentary environment (see section 4.2). Therefore, these three sites may be considered as an isochron-paleoelevation marker. We projected the position of these sites along a fault-normal profile to estimate relative elevation change. Unfortunately, no subsurface geophysical data exists for the EYOF, but the intersection of its linear trace with the topographic relief suggests a subvertical dip angle (Figures 2 and 3).

We allow models to extend up to the surface and searched in nested loops for the dip angle, slip, and down-dip depth of a planar fault that minimizes the weighted mean square root (WRMS),

Table 1
Radiocarbon Ages of Coastal Plain Sediments

Sample ID	Lab. ID	Site	Material	Elevation (m amtl)	^{14}C age (year BP)	Mean age (cal year BP)	Median age (cal year BP)	1s (cal year BP)	95.4% age range (cal year BP)
CH14-ELYO-T1-D11-B	Poz-65883	T1	charcoal	14.69	3,390 ± 90	3,648	3,643	115	3,414/3,871
CH14-ELYO-T1-D11-C	Poz-62933	T1	charcoal	14.75	2,210 ± 60	2,217	2,222	75	2,061/2,347
CH14-ELYO-T1-G10-A	Poz-62934	T1	charcoal	13.47	3,680 ± 35	4,018	4,021	56	3,903/4,143
CH14-ELYO-T1-H05-A	Poz-66009	T1	charcoal	12.77	3,500 ± 35	3,771	3,771	50	3,649/3,868
CH14-ELYO-T1-I01-A	Poz-62936	T1	charcoal	12.04	3,455 ± 30	3,729	3,719	57	3,640/3,828
CH14-ELYO-T1-K03-B	Poz-62937	T1	charcoal	11.04	3,780 ± 60	4,164	4,161	102	3,981/4,405
CH14-ELYO-T1-L01-A	Poz-66006	T1	charcoal	10.6	3,550 ± 35	3,833	3,844	60	3,720/3,960
CH14-ELYO-T1-L02-A	Poz-66007	T1	charcoal	10.92	3,525 ± 35	3,795	3,790	55	3,700/3,892
CH14-ELYO-T1-L03-A-T	Poz-66010	T1	plant remains	10.57	3,800 ± 50	4,195	4,192	90	3,999/4,406
CH14-ELYO-T1-L03-A-B	Poz-66062	T1	plant remains	10.49	3,865 ± 35	4,297	4,297	69	4,158/4,414
CH14-ELYO-T1-N02-A	Poz-62938	T1	charcoal	9.9	3,545 ± 30	3,825	3,838	55	3,719/3,911
CH14-ELYO-T4-A	Poz-66091	T4	charcoal	9.51	2,940 ± 35	3,092	3,096	58	2,976/3,207
CH14-ELYO-T4-C	Poz-66063	T4	charcoal	10.27	3,830 ± 40	4,242	4,234	78	4,097/4,408
CH14-ELYO-LO-A	Poz-62939	LG	charcoal	1.94	3,655 ± 30	3,984	3,975	56	3,893/4,085
JJ12-CONT-8-RC1	Poz-50371	LG	leaf fragment	2.12	3,195 ± 35	3,418	3,417	36	3,356/3,544

Note. BP: before present (year 1950). Calibrated using OxCal 4.2 (Ramsey, 2001) and ShCal13 (Reimer et al., 2009).
Abbreviations: T: trench; LG: lagoon; amtl: above mean tide level.

$$\mathrm{WRMS} = \sqrt{\sum \frac{(Z_{\mathrm{obs}} - Z_{\mathrm{mod}})^2}{Z_e^2} / \sum \frac{1}{Z_e^2}}$$

where Z_{obs} and Z_{mod} are the measured and modeled displacements, respectively, and Z_e is the error in the elevation estimate at each site. We searched for the best fitting model using the position and elevation of past sea level markers, allowing only for dip slip (rake=90°). Because the 4-ka isochron is represented by only three sites, which are not sufficient to estimate fault slip, we added two additional geomorphic markers of Holocene relative sea level (RSL) change, the inner edge of the coastal plain (foot of the Holocene coastal cliff), and the shoreline angle of the Holocene marine terrace (Figure S6). We estimated the displacement by subtracting the elevation of the lowest-elevation marker. We performed two modeling experiments: Model 1 using the Holocene inner edges and Model 2 using the Holocene terrace shoreline angles (Figure 10). All experiments were performed using the same model setup based on a 5 × 5 km^2 domain with a 10-m grid size.

3.5. Seismotectonic Segmentation and Coulomb Stress-Transfer Models

In order to test the relationship between slip distribution during megathrust earthquakes and upper-plate fault reactivation, we first mapped the relation of coseismic slip during the 2010 Maule earthquake (Moreno et al., 2012) and the distribution of residual gravity anomaly and residual bathymetry (Bassett et al., 2016; Bassett & Watts, 2015a; Bassett & Watts, 2015b). Based on these relationships, we defined three subsegments for the Maule rupture zone, which we then use to address the link between the EYOF and megathrust slip using coseismic static Coulomb stress transfer calculations (e.g., Freed, 2005; King et al., 1994). These models consider the stress interaction between the megathrust and the EYOF as receiver fault, which are included as dislocations in an elastic half space (Okada, 1985). We used the Coulomb 3 software (Lin & Stein, 2004) assuming an effective coefficient of friction of 0.4, Poisson ration of 0.25, and a Young's modulus of 10^{10} Pa, as used in similar studies (Cortés-Aranda et al., 2015). Depending on the slip distribution of the main fault, in this case the megathrust, upper-plate faults may response by reverse or normal motion, as suggested by field observations and modeling studies along the Chile margin (Li et al., 2014; Loveless et al., 2010; Melnick, Moreno, Motagh, et al., 2012). We selected three scenarios as input for the stress transfer models: (1) the slip distribution of the 2010 Maule earthquake (Moreno et al., 2012), (2) the slip deficit estimated by integrating the geodetic interseismic locking model back to the time of the last earthquake in 1835 (Melnick, Moreno, Cisternas, & Tassara, 2012), and for a series of synthetic megathrust ruptures (100-km wide and at 25-km depth) that mimic a single patch of high slip and have centroids located between

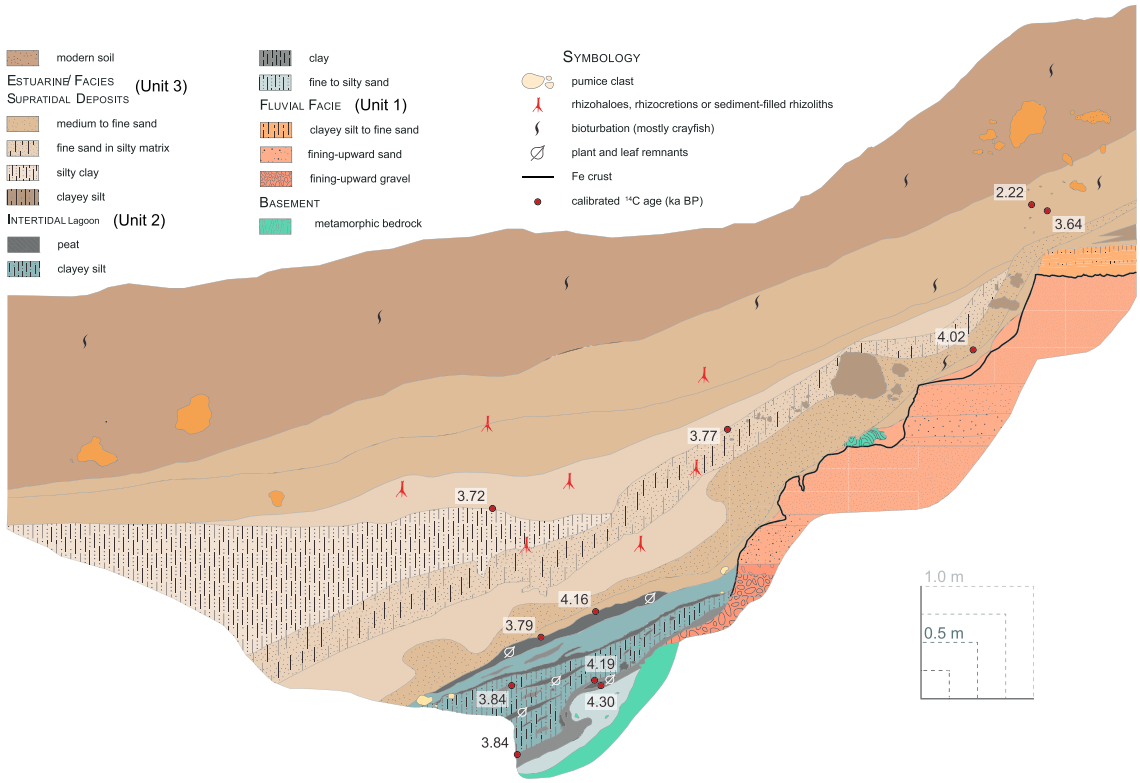

Figure 5. Log of principal trench T1 north wall. The red circles indicate location of radiocarbon samples labeled with calibrated age in ka BP.

38 and 33°S (Figures 12 and S7). For each of these input scenarios, we calculate the Coulomb Failure Stress change on the EYOF plane.

4. Results

4.1. Geometry of the EYOF

Geologic mapping based on LiDAR DTMs reveals that the EYOF consists of a series of NW-SE striking, right-stepping en échelon strands that extend for ~10 km inland from the coast (Figure 2). The surface trace of the EYOF is well defined along the western flank of the Coastal Cordillera but loses continuity at the coastal plain (Figure 3). We infer that the EYOF may extend farther offshore. The offset estimated from marine surfaces and from changes in thickness of Pleistocene siliceous sandstone across the fault suggest a SW dipping oblique normal fault with a sinistral strike-slip component. A halfgraben on the hanging wall contains an up to 60-m-thick synextensional sequence of siliceous sandstone and conglomerate of inferred Early Pleistocene age based on regional stratigraphic relationships and pinchouts (Figure 2). This age interpretation is furthermore based on thick soil profiles covering the deposits and deeply incised valleys, which contrast markedly with soils and incision profiles of marine terraces and deposits of MIS-5 and 7 age (Jara-Muñoz et al., 2015). NE dipping normal faults, antithetic to the main EYOF trace affect siliceous sands, exposed in a quarry and record displacements of between 2 and 3 m. Together with the en échelon traces of the EYOF, these secondary structures support the notion of a transtensional kinematic regime in this sector of the forearc.

Marine sediments dated as MIS-5e and MIS-5c, and associated with distinct terrace levels are offset by ~25 and ~10 m across the EYOF, respectively (Jara-Muñoz et al., 2015). However, no clear evidence of a recent scarp associated with young surface faulting could be found along the Holocene coastal plain (Figure 3), on either airborne and terrestrial LiDAR DTMs or in the field.

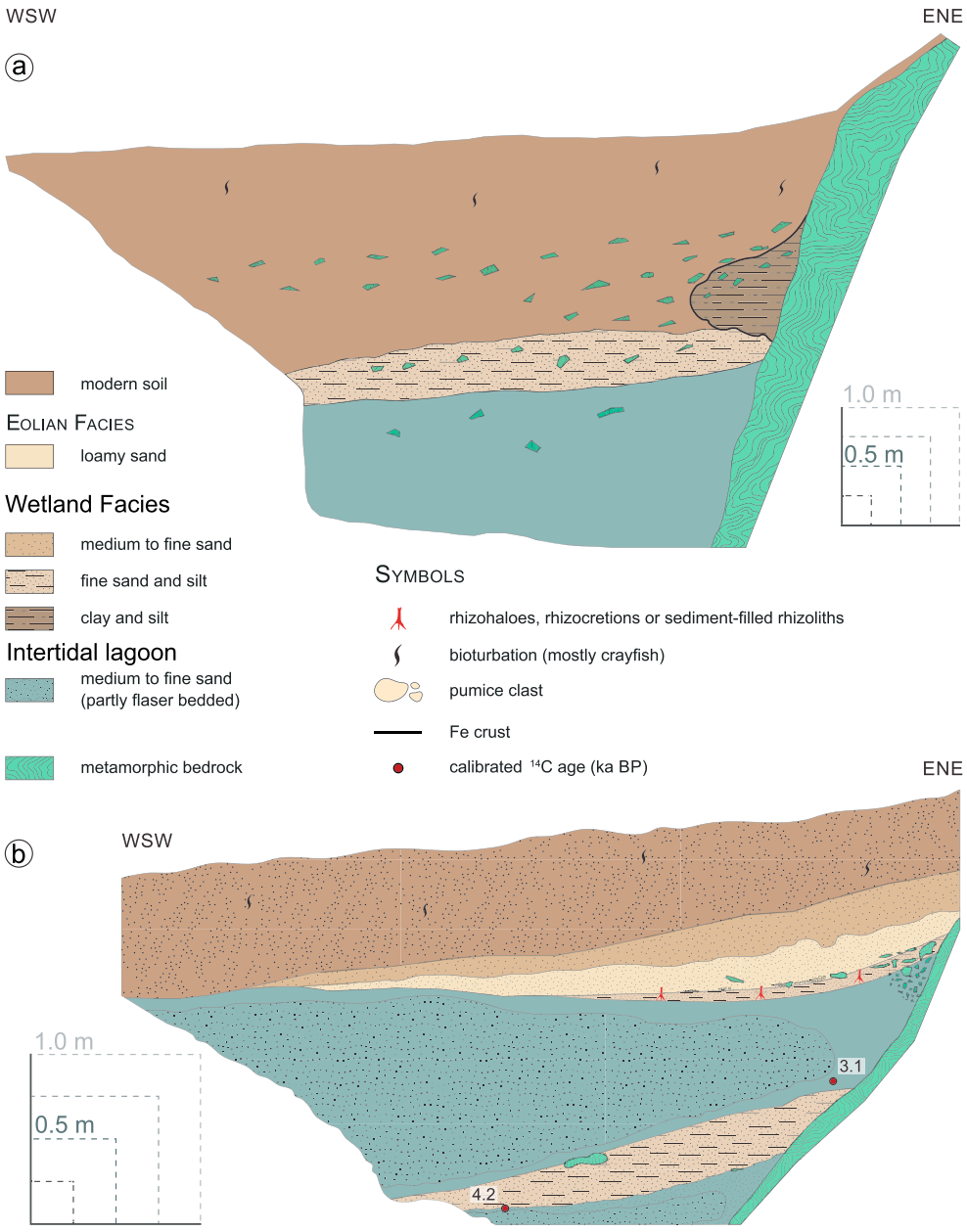

Figure 6. Log of auxiliary trenches T3 and T4 north walls. The red circles indicate location of radiocarbon ages labeled with calibrated ka BP.

4.2. Stratigraphy of the Holocene Coastal Plain

4.2.1. Principal Trench T1

This 12-m-long and up to 5-m-deep trench was excavated at ground surface elevations between 9.5 and 11.5 m amtl (location in Figure 3, trench log in Figure 5, photomosaic in Figure S2, and detailed description of sedimentary facies in Figure S3). The trench exposed the metamorphic bedrock at the base and a sedimentary sequence that may be grouped into three distinct lithostratigraphic units described below (from lower to upper exposures).

1. Unit 1 comprises a series of terrestrial, poorly consolidated coarse, sand and well-sorted gravels with horizontal bedding, normal grading, and well-sorted gravel with gently imbricated basal clasts immediately overlying the metamorphic bedrock. This unit lacks any evidence of bioturbation; it displays mottling

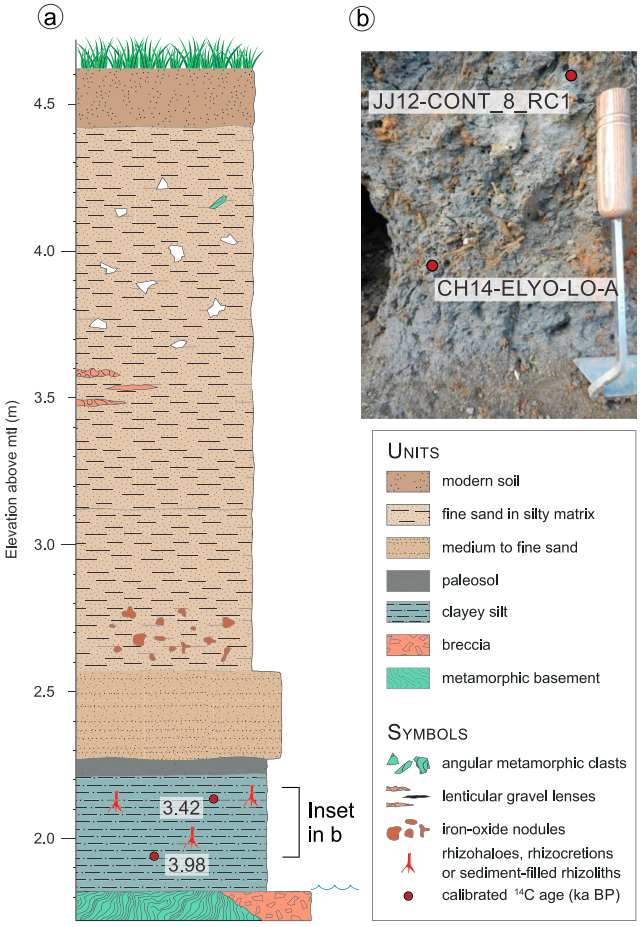

Figure 7. (a) Stratigraphic section of exposed coastal plain sediments along the northern lagoon shore (Location in Figure. 3). The red circles indicate location of radiocarbon ages labeled with calibrated ka BP. (b) Inset shows rhizoliths forming paleosoil at the top of the grey-bluish silty intertidal unit.

related to iron redox reactions and manganese precipitation. We interpreted this lower unit to be of fluvial and alluvial origin. This unit and the metamorphic bedrock are furthermore characterized by a stepped sequence of five distinct, decimeter-scale steps that have been sculpted at successively higher positions in a staircase arrangement (staircase profile with labeled step treads in Figure S5). Colluvial aprons (a wedge-shaped body deposited at the base of a cliff that tapers toward the hillslope), 0.5 m wide and 0.5 m thick formed by sediments of the lower fluvial unit cover debris slopes at the foot of each step. This staircase morphology is covered unconformably by onlapping strata of unit 2. The top contact surface of the staircase sequence is sealed by a laterally continuous, very resistant iron crust, which marks a zone of severed permeability gradient between this and the overlying units.

2. Unit 2 is an up to 2-m-thick sequence of organic-rich bluish-gray silty sediments that were deposited in a reducing environment. These sediments dip westward between 20 and 30° and progressively onlap onto the underlying unit 1 and the metamorphic basement. The lowermost bluish-gray facies comprise fine sand in a silty matrix with clay pockets and a few interspersed sharp-edged clasts of fractured greenschist. Small-scale soft-sediment deformation phenomena occur. This layer includes several lenses of dark peat, up to 15 cm thick. The peat lenses contain plant remains including entire leaves and small stems. Clasts of rounded pumice are additionally found scattered in the clay-silt layers. This horizon includes diatom species typically found at elevations in the upper part of the intertidal zone, around or slightly above the MHHW tidal datum (Table S1). We interpret that the sediments of this unit were deposited in a wetland environment that included marginal lagoon and intertidal marsh.
3. Unit 3 is an at least 2-m-thick sequence of fine reddish-brown silty-sand deposited in an oxidizing terrestrial environment. These seaward dipping sediments overlie unit 2 gradually in the lower part of the trench, and with sharply developed onlaps toward the top. A few embedded angular blocks of unit 1, intense crayfish bioturbation and contorted iron crusts are found scattered in this unit. We interpret this unit to be of eolian origin. This unit forms the C-horizon of an ~50- to 75-cm-thick soil with marginal rhizohalos and bioturbation.

The radiocarbon age of sediments in the principal trench T1 could be constrained by 13 samples that have median ages ranging from 2.2 to 4.2 cal ka BP (calibrated kiloyears Before Present) and span elevations between 9.9 and 14.9 m amtl, respectively. The Bayesian age-depth model suggests sedimentation rates of ~0.5 mm/year for the lower gray-blue silt with peat lenses and an acceleration to 5-10 mm/year for the overlying units (Figure 8).

4.2.2. Secondary Trenches and Lagoon Exposure

1. Trench T3 was excavated 50 m north and parallel to T4 (Figure 3). It exposed a 6-m-long and up to 3.5-m-deep sedimentary section onlapping onto metamorphic bedrock (Figure 6). The bottom of the trench (7.5 m amtl) exposes an ~1.5-m-thick unit of massive bluish-gray medium to fine sand with angular cobble-size clasts of the adjacent bedrock. The overlying unit consists of olive-gray to brown fine sand and silt separated by an abrupt contact. The lower sandy unit below may represent accumulation in a reducing depositional environment; the lenticular fine sand to silt layer on top corresponds to a more oxidizing environment. An up to 2-m-thick modern agricultural soil seals the sequence.
2. Trench T4 is located ~200 m north of T1 and exposed a 6-m-long and up to 3-m-deep sedimentary section laterally onlapping onto metamorphic bedrock. A lower, >1.2-m-thick unit consists of dark bluish-gray fine to medium sand with distinct flaser bedding. Interbedded is an 0.5-m-thick inclined lens of olive-brown fine sand with a silty matrix and centimeter-scale clay lenses and some boulder-size bedrock

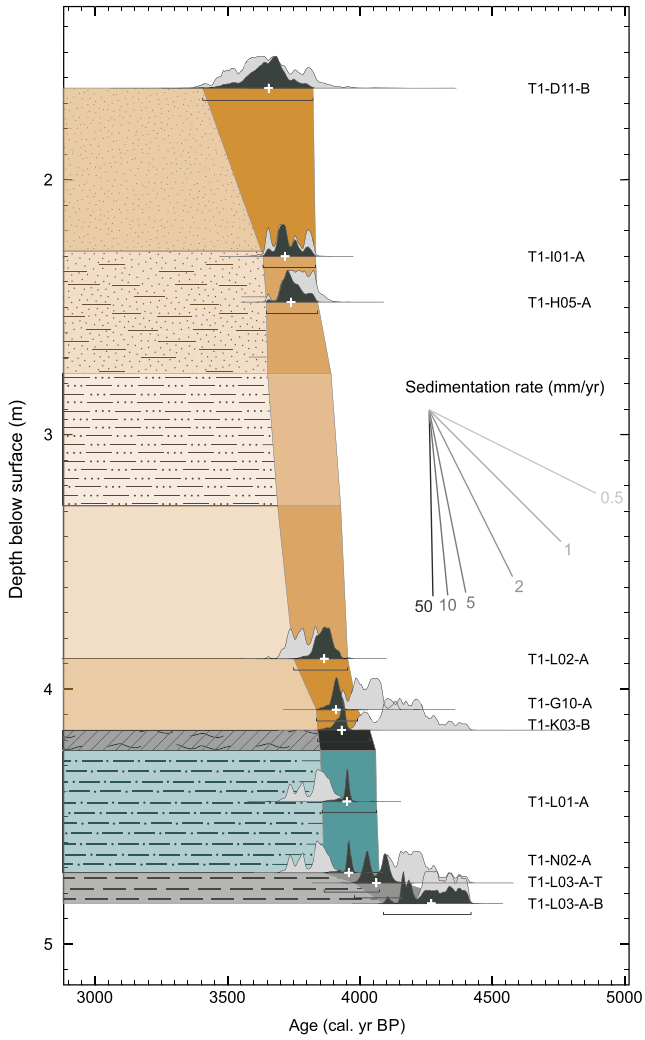

Figure 8. Age-depth model for the deposits exposed in principal trench T1. The filled gray curves denote sample probability density curves; the black curves show modeled distributions using a Bayesian approach (P-Sequence OxCal model, see text for details). The error bars represent the 99.7% confidence interval (2σ). The white crosses show modeled median ages depicting onset/termination of sedimentation.

fragments. Sparse organic material occurs predominantly at the stratigraphic boundaries. The silty sand layer also contains manganiferous rhizocretions and sediment-filled rhizoliths. A bent lens of loamy sand gradually covers both units tapering seaward and is covered by a well-developed agricultural soil with rootlets and rhizoturbation. Two radiocarbon samples constrain the age of sediments in trench T4 to an age range between 3.1 and 4.2 ka BP, at 9.5 and 10.3 m amtl, respectively.

3. Because of its proximity to the EYOF (Figure 3), trench T5 appeared to be a promising site to find evidences of surface-breaking fault ruptures. However, this 5-m-long and up to 4-m-deep trench exposed only a monotonous uniform dark brown organic-rich silt and loam grading into modern soil. The mature soil profile is partly leached, heavily bioturbated, and exposes slight to intense recent rhizoturbation. These sediments are analogous to the upper unit in T1, but with greater thickness. Because of the lack of datable material and intertidal stratigraphy, this trench was not logged in detail.
4. Holocene coastal plain sediments are exposed along the northern flank of a modern lagoon (Figures 3, 4e, and 7). A basal breccia overlies the metamorphic bedrock and is covered by a ~40-cm-thick layer of bluish-gray silt and clay with mottling and tubular plant stems and rhizoliths forming a mottled texture (Figure 7b). This unit features diatom assemblages indicative of deposition in the upper part of the intertidal zone, near MHHW (Table S1), and consists of a laminated and massive decimeter-scale bed that comprises fining-upward medium- to fine-sand sequence. The upper part of the exposure consists of an up to 1.8-m-thick sequence of fine sand with lenses of conglomerate formed by gravel-size fragments of angular metamorphic bedrock that transitions into modern soil. Charcoal and leaf fragments collected from the lower unit at 1.94 and 2.1 m amtl yielded ages of 4.0 and 3.4 cal ka BP (Figure 7b and Table 1).

The sedimentary units in T3 and T4 as well as the lagoon exposure are analogous to those found in T1, in facies, diatom assemblages, and radiocarbon ages, and we interpret them similarly as having been deposited in an environment that shifted gradually from a wetland and intertidal marsh to an aeolian backshore coastal plain. Aeolian accumulation was either larger at T5 or this site was located at a higher elevation ~4 ka ago precluding wetland sedimentation.

4.3. EYOF Holocene Slip Rate and Subsurface Geometry

Dislocation models of displaced stratigraphic and geomorphic markers were used to infer fault-slip rates of the EYOF (Figure 10). We obtained slip rates for different model setups. Model 1 (including the 4-ka MHHW isochron sites and the Holocene shoreline angles) suggests a slip rate of 5.6 mm/year for a 90°-dipping fault that extends down to 390-m depth, with a WRMS of 1.2 mm/year. Model 2 (including the isochron sites and Holocene inner edges) yielded a slip rate of 5.9 mm/year for a 90°-dipping fault extending from the surface to 510-m depth, with a WRMS of 0.4 mm/year. However, we cannot discard that these WRMS values underestimate the total epistemic uncertainty resulting from the lack of measurements in the hanging wall block.

The vertical deformation profiles predicted for both models across the EYOF (Figure 10c) are consistent with the topography and partly with the deformation pattern of the MIS-5e terrace. The subvertical dip angle obtained from the dislocation-model results is consistent with the regional geometry of the EYOF formed by en échelon fault traces (Figure 2). However, the ~500-m downdip depth for slip required to fit the narrow and steep tilt of the footwall block is not consistent with the >15-km-long surface trace of the EYOF (e.g., Gudmundsson, 1992). We infer that the fault responsible for the steep tilt of the Holocene coastal plain possibly forms part of a local negative flower structure, which is rooted in a deeper-reaching main fault strand,

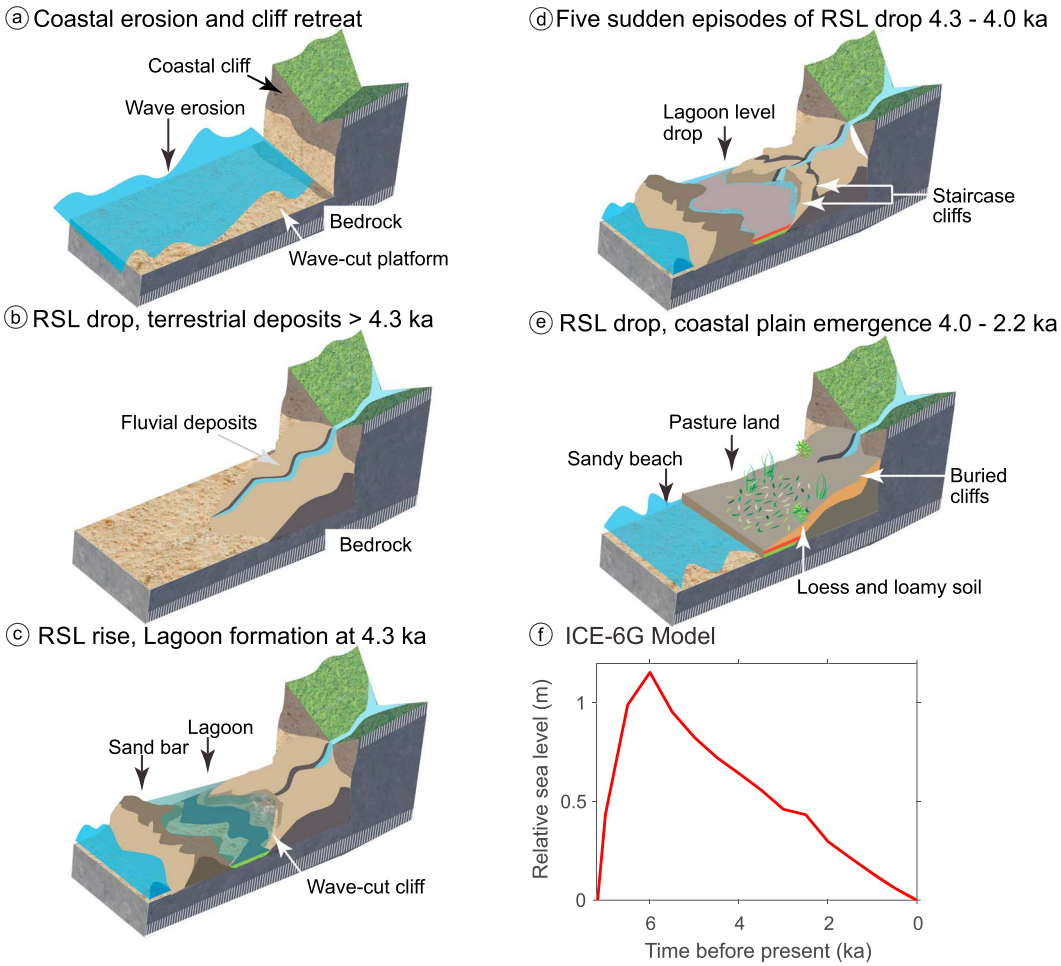

Figure 9. (a-e) Holocene landscape evolution of the coastal plain along the footwall block of the El Yolki Fault (see text for details). RSL: relative sea level. (f) RSL predicted by the ICE-6G_C model (Peltier et al., 2015) for the El Yolki region. Note the Middle Holocene highstand at 6 ka and steady regression.

or other branching fault geometry. This geometry may also provide an explanation for the lack of a clear surface scarp across the coastal plain in front of the intersection between the EYOF and the coastal mountain front (Figure 3) as slip may diffuse near the surface into several fault strands with complex geometry.

5. Discussion

5.1. Holocene Coastal Landscape Evolution and Slip Along the EYOF

Our stratigraphic, geochronologic, geomorphic, and microfossil results allow us to infer the evolution of five distinct episodes (described as E1-E5 below) of relative sea level (RSL) change since the mid-Holocene along the coastal plain of the EYOF footwall block (Figure 9). The amplitude and timescale of RSL change allow the attribution of a eustatic or tectonic mechanism for each episode.

1. E1: The coastal plain is bounded along its inner edge by a marked coastal cliff carved into metamorphic bedrock, which we associated with a protracted episode of slowly rising or steady RSL; these conditions led to retreat of the coastal cliff by wave erosion and development of an abrasion platform that generated the modern coastal plain. This episode coincided with the latest Pleistocene to Early Holocene and a Holocene minimum median age of 4.3 ka, which is constrained by the oldest age of the coastal plain sequence.
2. E2: After the carving of the coastal plain, RSL subsequently decreased, resulting in the deposition of terrestrial clastic sediments of fluvial origin; these form Unit 1 in trench T1 (Figures 5 and S5). These

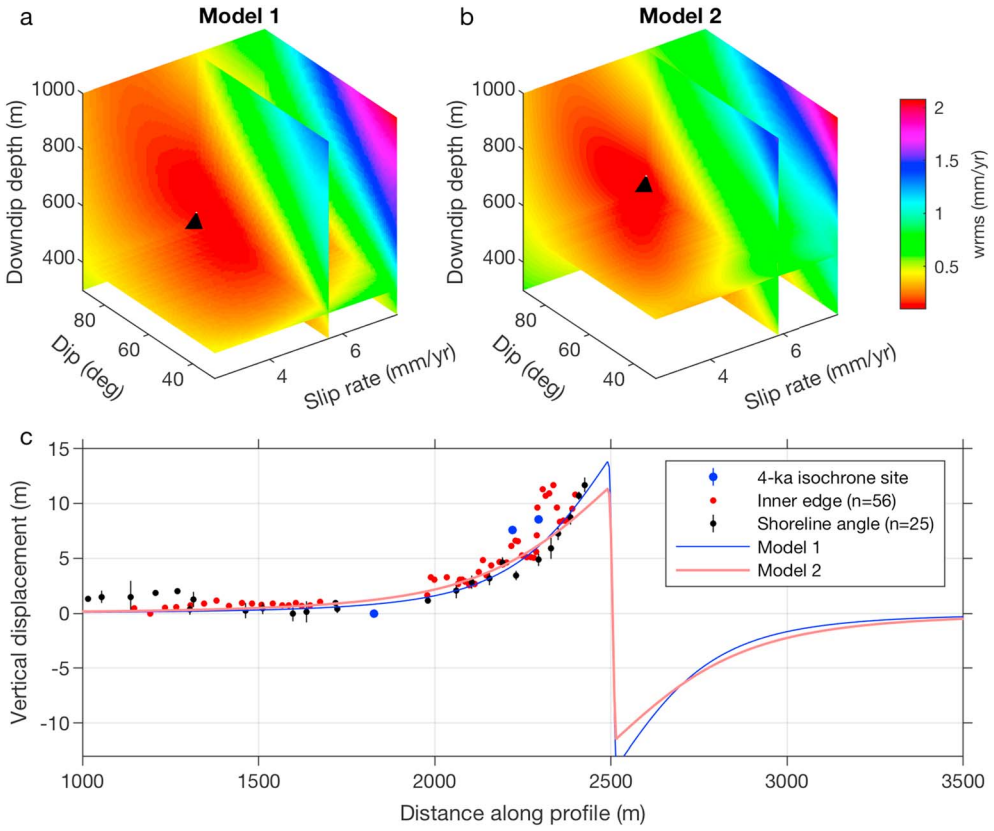

Figure 10. Holocene slip rate of the El Yolki Fault estimated from dislocation models of surface deformation markers by searching the combination of downdip rupture depth, fault dip, and slip rate that minimizes the weighted root mean square error (WRMS). (a) WRMS space for model 1, which includes the 4-ka isochron sites and the shoreline-angle measurements of the Holocene terrace. (b) WRMS space for model 2, including the 4-ka-old sites and the inner edges the Holocene cliff. See text for details. Note the similar slip rate from both models but different dips. (c) Vertical displacement along a fault-normal profile with projected data points and best fit models.

processes also took place before a minimum of 4.3 ka, and the inferred changes in RSL had an amplitude of at least ~4 m, which is necessary to account for the accommodation spaced required for the deposition of the fluvial sediments.

3. E3: This episode was characterized by RSL rise leading to closure of the coastal plain by a frontal sand bar and development of an inner lagoon, with deposition of bluish intertidal silt and peat in a reducing environment. The timing of E3 is constrained by six ages from trench T1 to between ~4.3 and 3.8 ka and by two ages at the lagoon outcrop and to between ~4.2 and 3.1 ka by two ages in trench T4. The age-depth model suggests a median age range between 4.25 and 3.85 ka (Figure 8). Diatom assemblages suggest that the silty sediments exposed at the base of T1 (sample L01-A) and the lagoon outcrop were deposited near MHHW. Moderate wave erosion (of much lower energy than during the previous episode or along the modern sandy beach) occurred along the eastern edge of the lagoon resulting in the retreat of a small cliff carved in the poorly consolidated fluvial sediments (deposited during E2).
4. E4: Subsequently and shortly after formation of the coastal plain lagoon, the five step-like scarps exposed in trench T1 forming an ~5-m-high staircase sequence of distinct steps were carved and rapidly covered by a veneer of supratidal fine sand. We associate this morphologic and sedimentary sequence with five sudden events of RSL drop and subdued wave erosion in a low-energy coastal environment. The occurrence of small, centimetric-scale colluvial aprons deposited at the foot of each cliff strongly suggests that subaerial exposure was short, probably between several decades and a few centuries at most. The timing of E4 is constrained by the six 4.3 to 3.8 ka ages obtained from the base of T1 and two 3.6-3.8 ka ages of the overlying supratidal layer. Although these ages nearly overlap within their 2-s ranges (Table 1), the

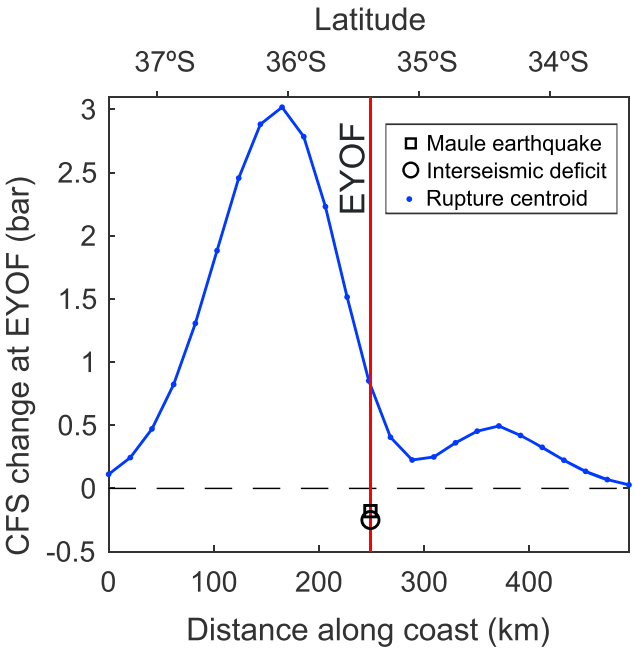

Figure 11. Models of stress transfer models from megathrust earthquake ruptures to the El Yolki fault (EYOF). The blue curve shows Coulomb Failure Stress (CFS) estimated at the EYOF resulting from synthetic megathrust ruptures (at 25-km depth and 100 km wide); the blue dots show rupture centroid. The red line shows projected position of the EYOF. The square shows CFS at the EYOF using the slip distribution of the 2010 Maule earthquake (Moreno et al., 2012); the black circle shows CFS estimated using the slip deficit calculated using the modern interseismic locking extrapolated back to the date of the last great earthquake in 1835 (Melnick, Moreno, Cisternas, & Tassara, 2012). Maps of CFS based on 2010 slip and 1835-2010 interseismic deficit as well as synthetic scenarios may be found in Figure S7.

temporal evolution deduced from the Bayesian age model (Figure 8) suggests a similar temporal framework. However, we cannot directly constrain the timing of individual RSL drop events and erosional step formation based on this model, but together with the geomorphic evidence (colluvial aprons), we interpret that these steps are microcliffs that were formed and subsequently abandoned in a relatively short period of time.

5. E5: The intertidal sequence described above was covered by supratidal fine to medium sand deposited in an aeolian environment implying partial closure of the lagoon. RSL rose rapidly resulting in deposition of ~2 m of intertidal lagoonal sediments with rapid sedimentation rates of ~8 mm/year, covering the five microcliffs and helping to preserve their geometry. After ~2.2 ka RSL continued to drop either episodically or continuously, resulting in complete emergence of the modern coastal plain and deposition of eolian sediments that are now covered by agricultural soils (Figures 8 and 9). We interpret the iron crust at the contact between units 1 and 2 to reflect groundwater flow and deposition along a permeability contrast in the sediment.

We infer that episodes E1-E3 were associated with eustatic sea level rise during the climatically controlled mid-Holocene sea level highstand (e.g., Melnick et al., 2018; Milne et al., 2005; Peltier et al., 2015). In south-central Chile, the highstand started before ~6 ka, judging by the oldest ages in the region (e.g., Dura et al., 2015; Isla et al., 2012; Stefer et al., 2010), and at El Yolki the end of the highstand is constrained by the oldest radiocarbon age of 4.1-4.4 ka (4.25 ka from Bayesian age-depth model; Figure 8), consistent with the age range obtained from dating coastal geomorphic markers in south-central Chile, and with global-scale model results (Peltier et al., 2015). Although no detailed Holocene RSL curve has been yet obtained for south-central Chile as of yet, the ICE-6G model (Peltier et al., 2015) suggests smooth changes in RSL over the Holocene with an amplitude of ~1-2 m (Figure 9f), which cannot explain our observations of RSL drop during E2. We therefore attribute E2 to local tectonic uplift likely associated with slip along the EYOF and resulting in >4 m of footwall uplift (Figures 10 and 11).

In turn, we interpret the five distinct microcliffs that formed during E4 as a series of RSL drop events associated with pulsed tectonic uplift. A possible scenario is the occurrence of a cluster of five coseismic uplift events associated with slip along the EYOF caused by crustal earthquakes. In addition to steady RSL rise, a shallow megathrust earthquake that ruptured domains A and B (Lay et al., 2012) may have caused metric-scale subsidence during this time interval; however, such coseismic subsidence is likely recovered by interseismic uplift considering the predominantly elastic behavior of the shallow portion of megathrust systems (e.g., Briggs et al., 2008). The fast uplift rate of ~4 mm/year inferred from the 4-ka MHHW isochron, which reaches an elevation of ~10 m at T1, suggests that slip along the EYOF has continued thereafter, but sedimentary and geomorphic evidence is absent from the geologic record, possibly because the rate of eustatic RSL change was either negative or positive but lower than the rate of tectonic uplift. The record of pulsed uplift associated with slip events along the EYOF is therefore fragmentary in light of the RSL changes controlled by a combination of tectonic and climatic processes.

Surface faulting associated with slip at depth propagating updip to a flower structure might occur across a complex array of fault strands, as inferred for transtensional and transpressional crustal faults (Harding, 1985) including those associated with the 2017 Kaikoura earthquake (e.g., Hamling et al., 2017; Hollingsworth et al., 2017; Wang et al., 2018). Complex surface fault geometries that merge at depth into a single narrower fault zone have been inferred for coastal faults in south-central Chile (Jara-Muñoz et al., 2017; Melnick & Echtler, 2006) and elsewhere (e.g., Ghisetti et al., 2018); this is apparently a common feature of upper-crustal structures such as the EYOF.

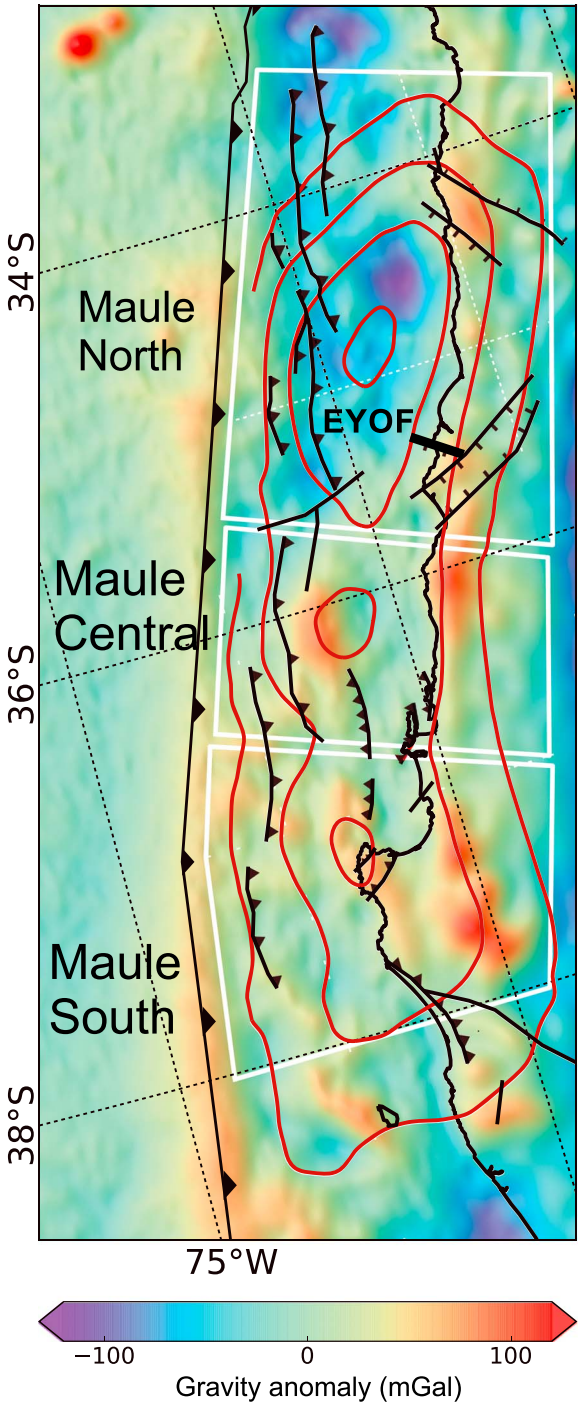

Figure 12. Residual gravity anomaly and seismotectonic segmentation model of the 2010 Maule earthquake rupture zone. The red contours show slip distribution of the 2010 Maule earthquake (Moreno et al., 2012). Quaternary faults modified from Jara-Muñoz et al. (2015).

5.2. Relationships Between Megathrust Earthquakes and EYOF Slip

Upper-plate faults such as the EYOF may be reactivated by a megathrust event when they are optimally oriented with respect to the tectonic stress regime imposed by coseismic slip (e.g., Gomberg & Sherrod, 2014). No evidence of recent deformation along the EYOF was found after the 2010 Maule earthquake, consistent with results from Coulomb stress-transfer models that suggested a negative stress change along the EYOF after the event (Figure 12). However, our paleoseismic results suggest extensional deformation along the EYOF in the recent past resulting in the geomorphic and stratigraphic manifestations of five closely spaced mid-Holocene seismic slip events, associated with footwall uplift. If these crustal earthquakes were indeed triggered by a megathrust event, as suggested by their extensional kinematics, the slip distribution of that event must have been significantly different from that of the Maule earthquake.

The Maule earthquake rupture was characterized by three distinct patches of high slip, which are correlated in space with patterns in the distribution of gravity anomalies and residual bathymetry (Figure 11). These relationships suggest that the Maule earthquake involved the rupture of three distinct asperities, which we define as subsegments, and that apparently are persistent and controlled by the long-term tectonic evolution and geologic structure of the margin. A relationship between such seismotectonic segments highlighted by correlations among geophysical data and geologic features, and the distribution of megathrust slip during great earthquakes has been suggested to exist at various subduction zone forearcs (Bassett & Watts, 2015b; Song & Simons, 2003; Wells et al., 2003), although the underlying physical processes still remain poorly understood. We test the hypothesis that slip events at the EYOF were triggered by megathrust earthquakes slipping mostly along the central Maule subsegment by computing Coulomb Stress change models for synthetic slip distributions characterized by ~100-km-wide ruptures (Figures 12 and S7). These synthetic slip distributions show positive stress changes along the EYOF, suggesting that crustal earthquakes on the EYOF might indeed be triggered by megathrust earthquakes. These earthquakes either ruptured only the central subsegment of the Maule rupture zone or had more slip in that area with respect to the surrounding subsegments (Figure 13).

The offset of MIS-5e and 5c terrace levels across the EYOF (Jara-Muñoz et al., 2015) suggests that fault slip rates integrated over time scales of an ~10^5 years are up to an order of magnitude slower than those estimated at the Holocene timescale (2-5 mm/year). This discrepancy has been observed for faults in continental interiors at multiple timescales (e.g., Friedrich et al., 2003); this has been attributed to secular variations (e.g., Chevalier et al., 2005), earthquake clusters associated with interactions among multiple adjacent and interconnected structures (e.g., Bennett et al., 2004; Dolan et al., 2007) or climatically controlled changes in surface loads (e.g., Hetzel & Hampel, 2005), as well as supercycle behavior at millennial time scales (Schlagenhauf et al., 2011), among others. The EYOF is adjacent to a larger fault system located immediately south at Carranza (Figure 1), which has a similar slip rate deduced from the vertical displacement of the MIS-5 levels (Jara-Muñoz et al., 2015); interactions among these systems could modulate slip rate variations at multimillennial timescale. However, another possibility to interpret these phenomena is modulation caused by variations in the distribution of coseismic slip during great megathrust earthquakes, which in turn would trigger slip of upper-plate faults such as the

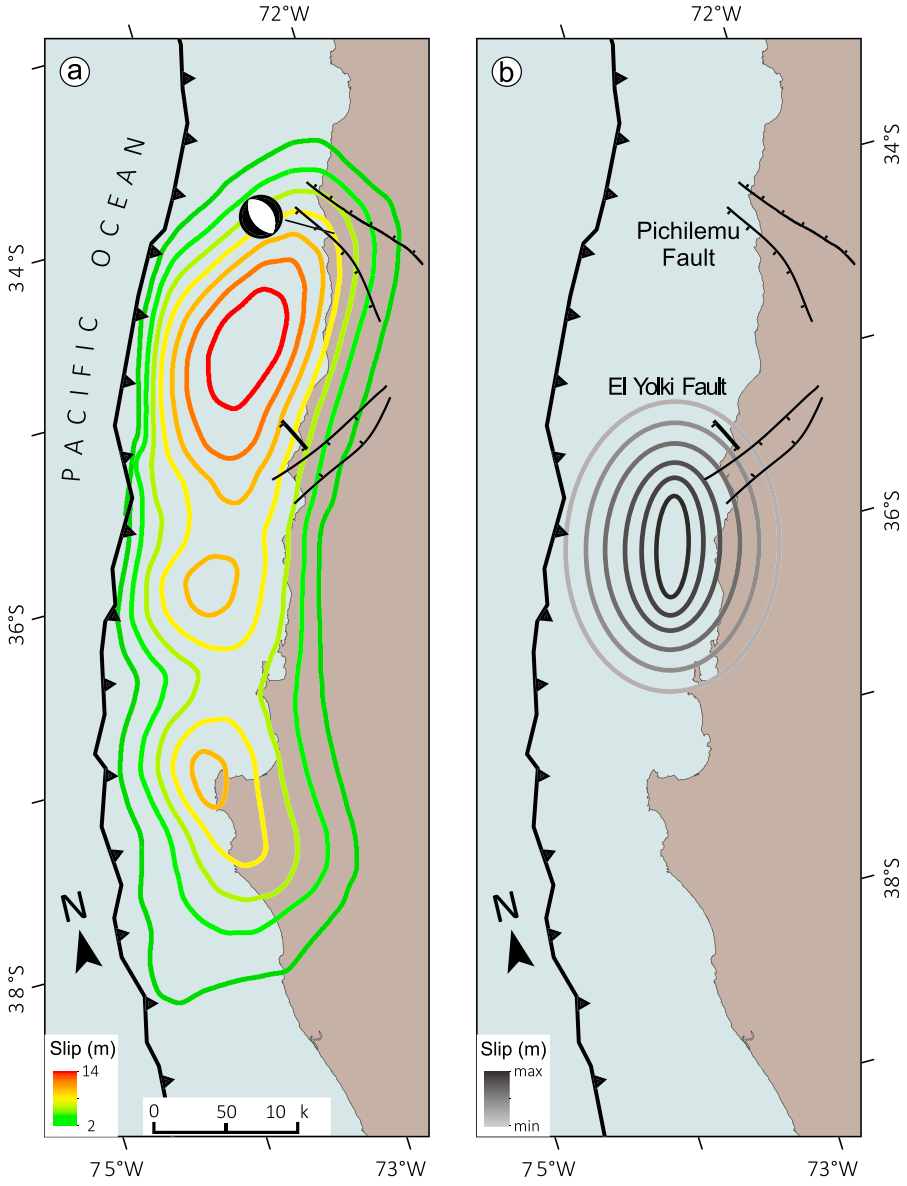

Figure 13. Conceptual model for triggering of upper-plate faults by megathrust earthquakes along the Maule segment. (a) Coseismic slip during the Maule earthquake (Moreno et al., 2012). Note the relationship between northern patch of high slip and the optimal orientation of the Pichilemu Fault for triggered slip. The black focal mechanism shows M7 earthquake on the Pichilemu Fault 11 days after the Maule mainshock. (b) Inferred slip distribution of a hypothetic megathrust earthquake that may trigger slip along the EYOF. Note that triggering requires slip in an area where the Maule slip was low.

EYOF. During historical times, giant M>9 super cycle earthquakes involving simultaneous rupture of several asperities as well as M>8 single-asperity earthquakes have occurred along the Andean megathrust, but the recurrence periods of such supercycles are poorly known. Variable megathrust earthquake recurrence could in turn modulate the slip rate on coastal faults, explaining the EYOF discrepancy over 10^3- to 10^5-year timescales.

The situation of the EYOF region and the Maule earthquake may be analogous to the segment of the Chile margin between 19 and 23°S. This entire region ruptured during a Mw~8.8 earthquake in 1877 that involved three distinct slip patches (Loveless et al., 2009) and during the Mw 8.1 Pisagua earthquake in 2014, when megathrust slip occurred along one of these patches (Loveless et al., 2016; Schurr et al., 2014). Interestingly, gravity anomaly maps of the 1877 and 2010 segments are similar and characterized by three

distinct high- and low-gravity patches of ~100 km in size (see Loveless et al., 2009, and Figure 11). The 2014 earthquake ruptured one of these patches and was associated with a half-moon pattern of coseismic extensional cracks surrounding the rupture (Loveless et al., 2016). The crack pattern surrounding the 2014 rupture may be analogous to the northern high-slip patch of the Maule earthquake, which is surrounded by Pichilemu, Carranza, and Pelluhue faults forming a half-moon pattern (Figure 1). This would imply a persistent seismotectonic segmentation of the megathrust and forearc, consistent with the gravity anomaly map that may be interpreted to reflect the tectonic evolution at ~10^6-year timescale. Our study has implications on estimating the hazard posed by hidden but potentially seismogenic coastal faults such as the EYOF, which are apparently modulated by the spatiotemporal evolution of the megathrust seismic cycle.

6. Conclusions

1. Deformed mid-Holocene coastal landforms along the south-central Chile active margin confirmed the existence of active extensional structures in the forearc. In the context of these structures, we studied the EYOF with airborne and terrestrial LiDAR scanning, geomorphic and geologic mapping, and paleoseismic trenching to unravel the evolution of coastal landscapes and the relation between crustal faulting and the megathrust earthquake cycle. Importantly, we combined stratigraphic and paleo-geomorphic observations from the trench exposures with stratigraphic data in surface cuts and landforms in the vicinity of the fault to assess the activity of the fault over time scales beyond the time window provided by the trench record.
2. Radiocarbon ages of plant remains and charcoal found in intertidal and supratidal sediments of the coastal plain suggest that the landscape changed from an open coastal environment before ~4.3 ka to an inner lagoon closed by a coastal sand bar between until ~3.3 ka. Eolian sedimentation covered the lagoon subsequently; the eolian sediments constituted the substratum for the formation of loamy soils that presently cover the area. Diatom assemblages of 4.0-ka-old intertidal sediments collected at two sites suggest deposition in the upper part of the tidal zone, approximately at the MHHW tidal level; these sites are now located at elevations of 1.9 and 10.5 m above modern mtl, and at distances approaching the EYOF along its footwall block. We interpret the differential elevation of this 4-ka isochrone level as a result of progressive back-tilting and footwall uplift in response to slip along the EYOF during the Holocene.
3. At El Yolki, Middle Holocene intertidal and supratidal sediments cover and preserve a sequence of five distinct, and temporally clustered erosive scarps, which we interpret as a staircase sequence of wave-cut landforms sculpted into the substrate by discrete pulses of RSL drops. The short wavelength (~1 km) of these deformed geomorphic features suggests that pulsed RSL fall events were likely associated with coseismic uplift during a cluster of crustal earthquakes along the EYOF, rather than with the effect of individual megathrust earthquakes.
4. The throw rate of the EYOF is ~2 mm/year estimated from geomorphic markers; dislocation models of fault slip embedded in an elastic half space suggest a slip rate of 5-6 mm/year, based the 4-ka isochrone, inner edge, and shoreline angle of the Holocene marine terrace. This relatively fast Holocene rate is unlikely to represent long-term fault behavior, and it is unlikely to have been sustained over time, because of the much lower displacement recorded by the MIS-5 terrace, which suggests a throw rate of <1 mm/year for the EYOF. The apparent variation in deformation rate might reflect paleo-earthquake clustering sampled over a short interval, aseismic slip, or variable modulation by megathrust earthquake super cycles.
5. Regional gravity anomalies suggest the forearc along the Maule earthquake segment may be subdivided into three subsegments with differences in crustal structure, which are coincident with, and probably control the three patches of high coseismic slip during the Maule event. This correlation suggests three distinct asperities that ruptured together during the Maule earthquake. Coulomb stress transfer models predict neutral to negative changes at the EYOF during the Maule earthquake, but positive changes for a synthetic slip distribution at the central subsegment. Thus, if the Middle Holocene cluster of crustal earthquakes associated with the EYOF was indeed triggered by megathrust earthquakes, their slip distribution was likely different from that of the Maule earthquake and possibly dominated by slip along the central subsegment.
6. Our study has implications for the understanding of potential earthquake clustering on crustal faults in response to megathrust earthquakes and possible variations of megathrust-slip distributions over various earthquake cycles within seismotectonic segments along the world's forearcs.

Acknowledgments

This study was supported by the Millennium Scientific Initiative (ICM) of the Chilean government through grant NC160025 "Millennium Nucleus CYCLO The Seismic Cycle Along Subduction Zones," Chilean National Fund for Development of Science and Technology (FONDECYT) grants 1150321, 1181479, and 1190258, German Science Foundation (DFG) grants ME 3157/4-2, JA 2860/1-1, and STR 373/30-1, VRID 216.025.038-1.0IN (UdeC), Natural Environment Research Council (NE/R00210X/1) with additional funding from the Department of Geography,Durham University, and IGCP Project 639 "Sea Level Change from Minutes to Millennia". E.G. is funded by the European Union/DurhamUniversity (COFUND). We thank F. Leiva for drafting Figure 9, D. Bassett for providing gravity anomaly grids, J. González-Carrasco for advice on CFS models, and constructive reviews by R. Briggs and J. Loveless. Samples are available from the authors on reasonable request. Data are available in the supplementary data sets and supporting information.

References

Allmendinger, R. W., & González, G. (2010). Invited review paper: Neogene to Quaternary tectonics of the coastal Cordillera, northern Chile. *Tectonophysics*, *495*(1-2), 93–110. https://doi.org/10.1016/j.tecto.2009.04.019

Allmendinger, R. W., González, G., Yu, J., Hoke, G., & Isacks, B. (2005). Trench-parallel shortening in the Northern Chilean Forearc: Tectonic and climatic implications. *GSA Bulletin*, *117*(1), 89–104. https://doi.org/10.1130/B25505.1

Angermann, D., Klotz, J., & Reigber, C. (1999). Space-geodetic estimation of the Nazca-South America Euler vector. *Earth and Planetary Science Letters*, *171*(3), 329–334. https://doi.org/10.1016/s0012-821x(99)00173-9

Aron, F., Allmendinger, R. W., Cembrano, J., González, G., & Yáñez, G. (2013). Permanent fore-arc extension and seismic segmentation: Insights from the 2010 Maule earthquake, Chile. *Journal of Geophysical Research: Solid Earth*, *118*, 724–739. https://doi.org/10.1029/2012JB009339

Audin, L., Lacan, P., Tavera, H., & Bondoux, F. (2008). Upper plate deformation and seismic barrier in front of Nazca subduction zone: The Chololo Fault System and active tectonics along the Coastal Cordillera, southern Peru. *Tectonophysics*, *459*(1-4), 174–185. https://doi.org/10.1016/j.tecto.2007.11.070

Bangs, N. L., & Cande, S. C. (1997). Episodic development of a convergent margin inferred from structures and processes along the southern Chile margin. *Tectonics*, *16*(3), 489–503. https://doi.org/10.1029/97TC00494

Bassett, D., Sandwell, D. T., Fialko, Y., & Watts, A. B. (2016). Upper-plate controls on co-seismic slip in the 2011 magnitude 9.0 Tohoku-oki earthquake. *Nature*, *531*(7592), 92–96. https://doi.org/10.1038/nature16945

Bassett, D., & Watts, A. B. (2015a). Gravity anomalies, crustal structure, and seismicity at subduction zones: 1. Seafloor roughness and subducting relief. *Geochemistry, Geophysics, Geosystems*, *16*, 1508–1540. https://doi.org/10.1002/2014GC005684

Bassett, D., & Watts, A. B. (2015b). Gravity anomalies, crustal structure, and seismicity at subduction zones: 2. Interrelationships between fore-arc structure and seismogenic behavior. *Geochemistry, Geophysics, Geosystems*, *16*, 1541–1576. https://doi.org/10.1002/2014GC005685

Bennett, R. A., Friedrich, A. M., & Furlong, K. P. (2004). Codependent histories of the San Andreas and San Jacinto fault zones from inversion of fault displacement rates. *Geology*, *32*(11), 961–964. https://doi.org/10.1130/G20806.1

Bowles, C. J., & Cowgill, E. (2012). Discovering marine terraces using airborne LiDAR along the Mendocino-Sonoma coast, northern California. *Geosphere*, *8*(2), 386–402. https://doi.org/10.1130/GES00702.1

Briggs, R. W., Sieh, K., Amidon, W. H., Galetzka, J., Prayudi, D., Suprihanto, I., et al. (2008). Persistent elastic behavior above a megathrust rupture patch: Nias island, West Sumatra. *Journal of Geophysical Research*, *113*, B12406. https://doi.org/10.1029/2008JB005684

Carvajal, M., Cisternas, M., & Catalán, P. (2017). Source of the 1730 Chilean earthquake from historical records: Implications for the future tsunami hazard on the coast of Metropolitan Chile. *Journal of Geophysical Research: Solid Earth*, *122*, 3648–3660. https://doi.org/10.1002/2017JB014063

Chevalier, M.-L., Ryerson, F., Tapponnier, P., Finkel, R., Van Der Woerd, J., Haibing, L., & Qing, L. (2005). Slip-rate measurements on the Karakorum fault may imply secular variations in fault motion. *Science*, *307*(5708), 411–414. https://doi.org/10.1126/science.1105466

Clarke, S., & Carver, G. (1992). Late Holocene tectonics and paleoseismicity, southern Cascadia subduction zone. *Science*, *255*(5041), 188–192. https://doi.org/10.1126/science.255.5041.188

Cortés, A. J., González, L., Binnie, S., Robinson, R., Freeman, S., & Vargas, E. (2012). Paleoseismology of the Mejillones Fault, northern Chile: Insights from cosmogenic 10Be and optically stimulated luminescence determinations. *Tectonics*, *31*, TC2017. https://doi.org/10.1029/2011TC002877

Cortés-Aranda, J., González, G., Rémy, D., & Martinod, J. (2015). Normal upper plate fault reactivation in northern Chile and the subduction earthquake cycle: From geological observations and static Coulomb Failure Stress (CFS) change. *Tectonophysics*, *639*, 118–131. https://doi.org/10.1016/j.tecto.2014.11.019

Cubas, N., Avouac, J.-P., Souloumiac, P., & Leroy, Y. (2013). Megathrust friction determined from mechanical analysis of the forearc in the Maule earthquake area. *Earth and Planetary Science Letters*, *381*, 92–103. https://doi.org/10.1016/j.epsl.2013.07.037

de Gelder, G., Fernández-Blanco, D., Melnick, D., Duclaux, G., Bell, R. E., Jara-Muñoz, J., et al. (2019). Lithospheric flexure and rheology determined by climate cycle markers in the Corinth Rift. *Scientific Reports*, *9*(1), 4260. https://doi.org/10.1038/s41598-018-36377-1

Dielforder, A., Vollstaedt, H., Vennemann, T., Berger, A., & Herwegh, M. (2015). Linking megathrust earthquakes to brittle deformation in a fossil accretionary complex. *Nature Communications*, *6*(1), 7504. https://doi.org/10.1038/ncomms8504

Dinther, Y. V., Gerya, T. V., Dalguer, L. A., Mai, P. M., Morra, G., & Giardini, D. (2013). The seismic cycle at subduction thrusts: Insights from seismo-thermo-mechanical models. *Journal of Geophysical Research: Solid Earth*, *118*, 6183–6202. https://doi.org/10.1002/2013JB010380

Dolan, J. F., Bowman, D. D., & Sammis, C. G. (2007). Long-range and long-term fault interactions in Southern California. *Geology*, *35*(9), 855–858. https://doi.org/10.1130/G23789A.1

Dura, T., Cisternas, M., Horton, B. P., Ely, L. L., Nelson, A. R., Wesson, R. L., & Pilarczyk, J. E. (2015). Coastal evidence for Holocene subduction-zone earthquakes and tsunamis in central Chile. *Quaternary Science Reviews*, *113*, 93–111. https://doi.org/10.1016/j.quascirev.2014.10.015

Dura, T., Horton, B. P., Cisternas, M., Ely, L. L., Hong, I., Nelson, A. R., et al. (2017). Subduction zone slip variability during the last millennium, south-central Chile. *Quaternary Science Reviews*, *175*, 112–137. https://doi.org/10.1016/j.quascirev.2017.08.023

Egbert, G. D., & Erofeeva, S. Y. (2002). Efficient inverse modeling of barotropic ocean tides. *Journal of Atmospheric and Oceanic Technology*, *19*(2), 183–204. https://doi.org/10.1175/1520-0426(2002)019<0183:EIMOBO>2.0.CO;2

Ewiak, O., Victor, P., & Oncken, O. (2015). Investigating multiple fault rupture at the Salar del Carmen segment of the Atacama Fault System (northern Chile): Fault scarp morphology and knickpoint analysis. *Tectonics*, *34*, 187–212. https://doi.org/10.1002/2014TC003599

Farias, M., Comte, D., Roecker, S., Carrizo, D., & Pardo, M. (2011). Crustal extensional faulting triggered by the 2010 Chilean earthquake: The Pichilemu Seismic Sequence. *Tectonics*, *30*, TC6010. https://doi.org/10.1029/2011TC002888

Farías, M., Vargas, G., Tassara, A., Carretier, S., Baize, S., Melnick, D., & Bataille, K. (2010). Land-level changes produced by the Mw 8.8 2010 Chilean earthquake. *Science*, *329*(5994), 916–916. https://doi.org/10.1126/science.1192094

Freed, A. M. (2005). Earthquake triggering by static, dynamic, and postseismic stress transfer. *Annual Review of Earth and Planetary Sciences*, *33*(1), 335–367. https://doi.org/10.1146/annurev.earth.33.092203.122505

Friedrich, A. M., Wernicke, B. P., Niemi, N. A., Bennett, R. A., & Davis, J. L. (2003). Comparison of geodetic and geologic data from the Wasatch region, Utah, and implications for the spectral character of Earth deformation at periods of 10 to 10 million years. *Journal of Geophysical Research*, *108*(B4), 2199. https://doi.org/10.1029/2001JB000682

Fuller, C. W., Willett, S. D., & Brandon, M. T. (2006). Formation of forearc basins and their influence on subduction zone earthquakes. *Geology*, *34*(2), 65–68. https://doi.org/10.1130/G21828.1

Garrett, E., Shennan, I., Watcham, E. P., & Woodroffe, S. A. (2013). Reconstructing paleoseismic deformation, 1: Modern analogues from the 1960 and 2010 Chilean great earthquakes. *Quaternary Science Reviews*, *75*, 11–21. https://doi.org/10.1016/j.quascirev.2013.04.007

Ghisetti, F. C., Johnston, M. R., Wopereis, P., & Sibson, R. H. (2018). Structural and morpho-tectonic evidence of Quaternary faulting within the Moutere Depression, South Island, New Zealand. *New Zealand Journal of Geology and Geophysics*, *61*(4), 461–479. https://doi.org/10.1080/00288306.2018.1502673

Glodny, J., Echtler, H., Figueroa, O., Franz, G., Gräfe, K., Kemnitz, H., et al. (2006). Long-term geological evolution and mass-flow balance of the South-Central Andes. In *The Andes* (pp. 401–428). Berlin, Heidelberg: Springer.

Glodny, J., Lohrmann, J., Echtler, H., Grafe, K., Seifert, W., Collao, S., & Figueroa, O. (2005). Internal dynamics of a paleoaccretionary wedge: Insights from combined isotope tectonochronology and sandbox modelling of the South-Central Chilean forearc. *Earth and Planetary Science Letters*, *231*(1-2), 23–39. https://doi.org/10.1016/j.epsl.2004.12.014

Gomberg, J., & Sherrod, B. (2014). Crustal earthquake triggering by modern great earthquakes on subduction zone thrusts. *Journal of Geophysical Research: Solid Earth*, *119*, 1235–1250. https://doi.org/10.1002/2012JB009826

González, G., Dunai, T., Carrizo, D., & Allmendinger, R. (2006). Young displacements on the Atacama Fault System, northern Chile from field observations and cosmogenic 21Ne concentrations. *Tectonics*, *25*, TC3006. https://doi.org/10.1029/2005TC001846

Gudmundsson, A. (1992). Formation and growth of normal faults at the divergent plate boundary in Iceland. *Terra Nova*, *4*(4), 464–471. https://doi.org/10.1111/j.1365-3121.1992.tb00582.x

Hamling, I. J., Hreinsdóttir, S., Clark, K., Elliott, J., Liang, C., Fielding, E., et al. (2017). Complex multifault rupture during the 2016 M w 7.8 Kaikōura earthquake, New Zealand. *Science*, *356*(6334). https://doi.org/10.1126/science.aam7194

Harding, T. (1985). Seismic characteristics and identification of negative flower structures, positive flower structures, and positive structural inversion. *AAPG Bulletin*, *69*(4), 582–600.

Hasegawa, A., Yoshida, K., Asano, Y., Okada, T., Iinuma, T., & Ito, Y. (2012). Change in stress field after the 2011 great Tohoku-Oki earthquake. *Earth and Planetary Science Letters*, *355*, 231–243.

Hervé, F., Munizaga, F., Parada, M., Brook, M., Pankhurst, R., Snelling, N., & Drake, R. (1988). Granitoids of the Coast Range of central Chile: geochronology and geologic setting. *Journal of South American Earth Sciences*, *1*(2), 185–194. https://doi.org/10.1016/0895-9811(88)90036-3

Hetzel, R., & Hampel, A. (2005). Slip rate variations on normal faults during glacial–interglacial changes in surface loads. *Nature*, *435*(7038), 81–84. https://doi.org/10.1038/nature03562

Hocking, E. P., Garrett, E., & Cisternas, M. (2017). Modern diatom assemblages from Chilean tidal marshes and their application for quantifying deformation during past great earthquakes. *Journal of Quaternary Science*, *32*(3), 396–415. https://doi.org/10.1002/jqs.2933

Hogg, A. G., Hua, Q., Blackwell, P. G., Niu, M., Buck, C. E., Guilderson, T. P., et al. (2013). SHCal13 Southern Hemisphere calibration, 0–50,000 years cal BP. *Radiocarbon*, *55*(4), 1889–1903. https://doi.org/10.2458/azu_js_rc.55.16783

Hollingsworth, J., Ye, L., & Avouac, J. P. (2017). Dynamically triggered slip on a splay fault in the Mw 7.8, 2016 Kaikoura (New Zealand) earthquake. *Geophysical Research Letters*, *44*, 3517–3525. https://doi.org/10.1002/2016GL072228

Isla, F. I., Flory, J. Q., Martínez, C., Fernández, A., & Jaque, E. (2012). The evolution of the Bío Bío delta and the coastal plains of the Arauco Gulf, Bío Bío Region: the Holocene sea-level curve of Chile. *Journal of Coastal Research*, *28*(1), 102–111.

Jara-Muñoz, J., Melnick, D., Brill, D., & Strecker, M. (2015). Segmentation of the 2010 Maule Chile earthquake rupture from a joint analysis of uplifted marine terraces and seismic-cycle deformation patterns. *Quaternary Science Reviews*, *113*, 171–192. https://doi.org/10.1016/j.quascirev.2015.01.005

Jara-Muñoz, J., Melnick, D., & Strecker, M. R. (2016). TerraceM: A MATLAB® tool to analyze marine and lacustrine terraces using high-resolution topography. *Geosphere*, *12*(1), 176–195. https://doi.org/10.1130/GES01208.1

Jara-Muñoz, J., Melnick, D., Zambrano, P., Rietbrock, A., Gonzalez, J., Argandona, B., & Strecker, M. R. (2017). Quantifying offshore forearc deformation and splay-fault slip using Pleistocene drowned shorelines, Arauco Bay, Chile. *Journal of Geophysical Research: Solid Earth*, *122*, 4529–4558. https://doi.org/10.1002/2016JB013339

Juggins, S. (2007). C2: Software for ecological and palaeoecological data analysis and visualisation (user guide version 1.5), Newcastle upon Tyne: Newcastle University, 77.

King, G. C., Stein, R. S., & Lin, J. (1994). Static stress changes and the triggering of earthquakes. *Bulletin of the Seismological Society of America*, *84*(3), 935–953.

Lavenu, A., & Cembrano, J. (1999). Compressional-and transpressional-stress pattern for Pliocene and Quaternary brittle deformation in fore arc and intra-arc zones (Andes of Central and Southern Chile). *Journal of Structural Geology*, *21*(12), 1669–1691. https://doi.org/10.1016/S0191-8141(99)00111-X

Lavenu, A., & Encinas, A. (2005). Deformación frágil de los depósitos neógenos de la cuenca de Navidad (Cordillera de la Costa, 34 S, Chile central). *Revista geológica de Chile*, *32*(2), 229–248.

Lay, T., Kanamori, H., Ammon, C. J., Koper, K. D., Hutko, A. R., Ye, L., et al. (2012). Depth-varying rupture properties of subduction zone megathrust faults. *Journal of Geophysical Research*, *117*, B04311. https://doi.org/10.1029/2011JB009133

Li, S., Moreno, M., Rosenau, M., Melnick, D., & Oncken, O. (2014). Splay fault triggering by great subduction earthquakes inferred from finite element models. *Geophysical Research Letters*, *41*, 385–391. https://doi.org/10.1002/2013GL058598

Lin, J., & Stein, R. S. (2004). Stress triggering in thrust and subduction earthquakes and stress interaction between the southern San Andreas and nearby thrust and strike-slip faults. *Journal of Geophysical Research*, *109*, B02303. https://doi.org/10.1029/2003JB002607

Lin, N., Sladen, A., Ortega-Culaciati, F., Simons, M., Avouac, J. P., Fielding, E. J., et al. (2013). Coseismic and postseismic slip associated with the 2010 Maule Earthquake, Chile: Characterizing the Arauco Peninsula barrier effect. *Journal of Geophysical Research: Solid Earth*, *118*, 3142–3159. https://doi.org/10.1002/jgrb.50207

Lin, Y.-S., Chuang, Y.-R., Shyu, J. B. H., González, G., Shen, C.-C., Lo, C.-H., & Liou, Y.-H. (2016). Structural characteristics of an active fold-and-thrust system in the southeastern Atacama Basin, northern Chile. *Tectonophysics*, *685*, 44–59. https://doi.org/10.1016/j.tecto.2016.07.015

Lomnitz, C. (2004). Major Earthquakes of Chile: A Historical Survey, 1535-1960. *Seismological Research Letters*, *75*(3), 368–378. https://doi.org/10.1785/gssrl.75.3.368

Loveless, J. P., Allmendinger, R. W., Pritchard, M. E., Garroway, J. L., & González, G. (2009). Surface cracks record long-term seismic segmentation of the Andean margin. *Geology*, *37*(1), 23–26. https://doi.org/10.1130/G25170A.1

Loveless, J. P., Allmendinger, R. W., Pritchard, M. E., & González, G. (2010). Normal and reverse faulting driven by the subduction zone earthquake cycle in the northern Chilean fore arc. *Tectonics*, *29*, TC2001. https://doi.org/10.1029/2009TC002465

Loveless, J. P., Scott, C. P., Allmendinger, R. W., & González, G. (2016). Slip distribution of the 2014 Mw= 8.1 Pisagua, northern Chile, earthquake sequence estimated from coseismic fore-arc surface cracks. *Geophysical Research Letters*, *43*, 10,134–10,141. https://doi.org/10.1002/2016GL070284

Marquardt, C., Lavenu, A., Ortlieb, L., Godoy, E., & Comte, D. (2004). Coastal neotectonics in Southern Central Andes: Uplift and deformation of marine terraces in Northern Chile (27°S). *Tectonophysics*, *394*(3-4), 193–219. https://doi.org/10.1016/j.tecto.2004.07.059

Martin, M. W., Kato, T. T., Rodriguez, C., Godoy, E., Duhart, P., McDonough, M., & Campos, A. (1999). Evolution of the late Paleozoic accretionary complex and overlying forearc-magmatic arc, south central Chile (38°-41°S): Constraints for the tectonic setting along the southwestern margin of Gondwana. *Tectonics*, *18*(4), 582–605. https://doi.org/10.1029/1999TC900021

McCaffrey, R., & Goldfinger, C. (1995). Forearc deformation and great subduction earthquakes: implications for Cascadia offshore earthquake potential. *Science*, *267*(5199), 856–859. https://doi.org/10.1126/science.267.5199.856

Melnick, D., Bookhagen, B., Echtler, H. P., & Strecker, M. R. (2006). Coastal deformation and great subduction earthquakes, Isla Santa Maria, Chile (37 degrees S). *Geological Society of America Bulletin*, *118*(11-12), 1463–1480. https://doi.org/10.1130/b25865.1

Melnick, D., Bookhagen, B., Strecker, M. R., & Echtler, H. P. (2009). Segmentation of megathrust rupture zones from fore-arc deformation patterns over hundreds to millions of years, Arauco peninsula, Chile. *Journal of Geophysical Research*, *114*, B01407. https://doi.org/10.1029/2008JB005788

Melnick, D., Cisternas, M., Moreno, M., & Norambuena, R. (2012). Estimating coseismic coastal uplift with an intertidal mussel: Calibration for the 2010 Maule Chile earthquake (M w= 8.8). *Quaternary Science Reviews*, *42*, 29–42. https://doi.org/10.1016/j.quascirev.2012.03.012

Melnick, D., & Echtler, H. P. (2006). Inversion of forearc basins in south-central Chile caused by rapid glacial age trench fill. *Geology*, *34*(9), 709–712. https://doi.org/10.1130/g22440.1

Melnick, D., Garrett, E., & Jara-Muñoz, J. (2018). Quantifying the timing and amplitude of Holocene relative sea level in south-central Chile using geomorphology and stratigraphy. In *IGCP Project 639 "Sea-Level Change from Minutes to Millennia*," (pp. 101-102). Taranto, Italy.

Melnick, D., Moreno, M., Cisternas, M., & Tassara, A. (2012). Darwin seismic gap closed by the 2010 Maule earthquake. *Andean Geology*, *39*(3), 558–563.

Melnick, D., Moreno, M., Motagh, M., Cisternas, M., & Wesson, R. L. (2012). Splay fault slip during the M w 8.8 2010 Maule Chile earthquake. *Geology*, *40*(3), 251–254. https://doi.org/10.1130/G32712.1

Melnick, D., Yildirim, C., Hilemann, C., Garcin, Y., Çiner, A., Pérez-Gussinyé, M., & Strecker, M. R. (2017). Slip along the Sultanhanı Fault in Central Anatolia from deformed Pleistocene shorelines of palaeo-lake Konya and implications for seismic hazards in low strain regions. *Geophysical Journal International*, *209*(3), 1431–1454. https://doi.org/10.1093/gji/ggx074

Meltzner, A. J., Sieh, K., Abrams, M., Agnew, D. C., Hudnut, K. W., Avouac, J. P., & Natawidjaja, D. H. (2006). Uplift and subsidence associated with the great Aceh-Andaman earthquake of 2004. *Journal of Geophysical Research*, *111*, B02407. https://doi.org/10.1029/2005JB003891

Milne, G. A., Long, A. J., & Bassett, S. E. (2005). Modelling Holocene relative sea-level observations from the Caribbean and South America. *Quaternary Science Reviews*, *24*(10-11), 1183–1202. https://doi.org/10.1016/j.quascirev.2004.10.005

Mordojovich, C. (1981). In M. T. Halbouty (Ed.), *Sedimentary basins of Chilean Pacific Offshore, in Energy Resources of the Pacific Region* (pp. 63–82). AAPG Studies in Geology.

Moreno, M., Melnick, D., Rosenau, M., Baez, J., Klotz, J., Oncken, O., et al. (2012). Toward understanding tectonic control on the M w 8.8 2010 Maule Chile earthquake. *Earth and Planetary Science Letters*, *321*, 152–165.

Okada, Y. (1985). Surface deformation due to shear and tensile faults in a half-space. *Bulletin of the Seismological Society of America*, *75*(4), 1135–1154.

Palmer, A. J., & Abbott, W. H. (1986). Diatoms as indicators of sea-level change. In *Sea-level Research* (pp. 457–487). Dordrecht: Springer.

Park, J.-O., Tsuru, T., Kodaira, S., Cummins, P. R., & Kaneda, Y. (2002). Splay fault branching along the Nankai subduction zone. *Science*, *297*(5584), 1157–1160. https://doi.org/10.1126/science.1074111

Peltier, W., Argus, D., & Drummond, R. (2015). Space geodesy constrains ice age terminal deglaciation: The global ICE-6G_C (VM5a) model. *Journal of Geophysical Research: Solid Earth*, *120*, 450–487. https://doi.org/10.1002/2014JB011176

Pérez, A., Ruiz, J., Vargas, G., Rauld, R., Rebolledo, S., & Campos, J. (2014). Improving seismotectonics and seismic hazard assessment along the San Ramón Fault at the eastern border of Santiago city, Chile. *Natural Hazards*, *71*(1), 243–274. https://doi.org/10.1007/s11069-013-0908-3

Plafker, G. (1965). Tectonic deformation associated with the 1964 Alaska earthquake. *Science*, *148*(3678), 1675–1687. https://doi.org/10.1126/science.148.3678.1675

Ramsey, C. B. (1995). Radiocarbon calibration and analysis of stratigraphy: the OxCal program. *Radiocarbon*, *37*(2), 425–430. https://doi.org/10.1017/S0033822200030903

Ramsey, C. B. (2001). Development of the radiocarbon calibration program. *Radiocarbon*, *43*(2A), 355–363.

Rehak, K., Niedermann, S., Preusser, F., Strecker, M. R., & Echtler, H. P. (2010). Late Pleistocene landscape evolution in south-central Chile constrained by luminescence and stable cosmogenic nuclide dating. *Bulletin*, *122*(7-8), 1235–1247.

Rehak, K., Strecker, M. R., & Echtler, H. P. (2008). Morphotectonic segmentation of an active forearc, 37–41 S, Chile. *Geomorphology*, *94*(1-2), 98–116. https://doi.org/10.1016/j.geomorph.2007.05.002

Reimer, P. J., Baillie, M. G., Bard, E., Bayliss, A., Beck, J. W., Blackwell, P. G., et al. (2009). IntCal09 and Marine09 radiocarbon age calibration curves, 0-50,000 years cal BP. *Radiocarbon*, *51*(4), 1111–1150.

Resor, P. G. (2008). Deformation associated with a continental normal fault system, western Grand Canyon, Arizona. *Geological Society of America Bulletin*, *120*(3-4), 414–430. https://doi.org/10.1130/B26107.1

Rosenau, M., Lohrmann, J., & Oncken, O. (2009). Shocks in a box: An analogue model of subduction earthquake cycles with application to seismotectonic forearc evolution. *Journal of Geophysical Research*, *114*, B014109. https://doi.org/10.1029/2008JB005665

Ruiz, J. A., Hayes, G. P., Carrizo, D., Kanamori, H., Socquet, A., & Comte, D. (2014). Seismological analyses of the 2010 March 11, Pichilemu, Chile M w 7.0 and M w 6.9 coastal intraplate earthquakes. *Geophysical Journal International*, *197*(1), 414–434. https://doi.org/10.1093/gji/ggt513

Ryder, I., Rietbrock, A., Kelson, K., Bürgmann, R., Floyd, M., Socquet, A., et al. (2012). Large extensional aftershocks in the continental forearc triggered by the 2010 Maule earthquake, Chile. *Geophysical Journal International*, *188*(3), 879–890. https://doi.org/10.1111/j.1365-246X.2011.05321.x

Schlagenhauf, A., Manighetti, I., Benedetti, L., Gaudemer, Y., Finkel, R., Malavieille, J., & Pou, K. (2011). Earthquake supercycles in Central Italy, inferred from 36Cl exposure dating. *Earth and Planetary Science Letters*, *307*(3-4), 487–500. https://doi.org/10.1016/j.epsl.2011.05.022

Schurr, B., Asch, G., Hainzl, S., Bedford, J., Hoechner, A., Palo, M., et al. (2014). Gradual unlocking of plate boundary controlled initiation of the 2014 Iquique earthquake. *Nature*, *512*(7514), 299–302. https://doi.org/10.1038/nature13681

Shennan, I., Long, A., Rutherford, M., Green, F., Innes, J., Lloyd, J., et al. (1996). Tidal marsh stratigraphy, sea-level change and large earthquakes, I: A 5000 year record in Washington, USA. *Quaternary Science Reviews*, *15*(10), 1023–1059. https://doi.org/10.1016/S0277-3791(96)00007-8

Sherrod, B., & Gomberg, J. (2014). Crustal earthquake triggering by pre-historic great earthquakes on subduction zone thrusts. *Journal of Geophysical Research: Solid Earth*, *119*, 1273–1294. https://doi.org/10.1002/2013JB010635

Song, T.-R. A., & Simons, M. (2003). Large trench-parallel gravity variations predict seismogenic behavior in subduction zones. *Science*, *301*(5633), 630–633. https://doi.org/10.1126/science.1085557

Stefer, S., Moernaut, J., Melnick, D., Echtler, H. P., Arz, H. W., Lamy, F., et al. (2010). Forearc uplift rates deduced from sediment cores of two coastal lakes in south-central Chile. *Tectonophysics*, *495*(1-2), 129–143. https://doi.org/10.1016/j.tecto.2009.05.006

Ten Brink, U., & Lin, J. (2004). Stress interaction between subduction earthquakes and forearc strike-slip faults: Modeling and application to the northern Caribbean plate boundary. *Journal of Geophysical Research*, *109*, B12310. https://doi.org/10.1029/2004JB003031

Toda, S., & Tsutsumi, H. (2013). Simultaneous reactivation of two, subparallel, inland normal faults during the Mw 6.6 11 April 2011 Iwaki earthquake triggered by the Mw 9.0 Tohoku-oki, Japan, earthquake. *Bulletin of the Seismological Society of America*, *103*(2B), 1584–1602. https://doi.org/10.1785/0120120281

Tong, X., Sandwell, D., Luttrell, K., Brooks, B., Bevis, M., Shimada, M., et al. (2010). The 2010 Maule, Chile earthquake: Downdip rupture limit revealed by space geodesy. *Geophysical Research Letters*, *37*, L24311. https://doi.org/10.1029/2010GL045805

Upton, P., Koons, P. O., & Eberhart-Phillips, D. (2003). Extension and partitioning in an oblique subduction zone, New Zealand: Constraints from three-dimensional numerical modeling. *Tectonics*, *22*(6), 1068. https://doi.org/10.1029/2002TC001431

Vargas, G., Klinger, Y., Rockwell, T., Forman, S., Rebolledo, S., Baize, S., et al. (2014). Probing large intraplate earthquakes at the west flank of the Andes. *Geology*, *42*(12), 1083–1086. https://doi.org/10.1130/G35741.1

Vargas, G., Rebolledo, S., Sepúlveda, S. A., Lahsen, A., Thiele, R., Townley, B., et al. (2013). Submarine earthquake rupture, active faulting and volcanism along the major Liquiñe-Ofqui Fault Zone and implications for seismic hazard assessment in the Patagonian Andes. *Andean Geology*, *40*(1), 141–171.

Vos, P. C., & de Wolf, H. (1993). *Diatoms as a tool for reconstructing sedimentary environments in coastal wetlands: Methodological aspects, paper presented at Twelfth International Diatom Symposium*. Dordrecht: Springer.

Wang, D., Chen, Y., Wang, Q., & Mori, J. (2018). Complex rupture of the 13 November 2016 Mw 7.8 Kaikoura, New Zealand earthquake: Comparison of high-frequency and low-frequency observations. *Tectonophysics*, *733*, 100–107. https://doi.org/10.1016/j.tecto.2018.02.004

Wang, K., & Hu, Y. (2006). Accretionary prisms in subduction earthquake cycles: The theory of dynamic Coulomb wedge. *Journal of Geophysical Research*, *111*, B06410. https://doi.org/10.1029/2005JB004094

Wells, R. E., Blakely, R. J., Sugiyama, Y., Scholl, D. W., & Dinterman, P. A. (2003). Basin-centered asperities in great subduction zone earthquakes: A link between slip, subsidence, and subduction erosion? *Journal of Geophysical Research*, *108*(B10), 2507. https://doi.org/10.1029/2002JB002072

Wesson, R., Melnick, D., Cisternas, M., Moreno, M., & Ely, L. (2015). Vertical deformation through a complete seismic cycle at Isla Santa María, Chile. *Nature Geoscience*, *8*, 546–511.

Willner, A. P. (2005). Pressure-temperature evolution of a Late Palaeozoic paired metamorphic belt in north-central Chile (34°-35°30′S). *Journal of Petrology*, *46*(9), 1805–1833. https://doi.org/10.1093/petrology/egi035

Erratum

In the originally published version of this article, Figure 5 and Figure 6 were transposed. This error has been corrected, and this may be considered the authoritative version of record.